NASA Technical Memorandum 4774

Effect of Actuated Forebody Strakes on the Forebody Aerodynamics of the NASA F-18 HARV

David F. Fisher, Daniel G. Murri, Wendy R. Lanser

October 1996

NASA Technical Memorandum 4774

Effect of Actuated Forebody Strakes on the Forebody Aerodynamics of the NASA F-18 HARV

David F. Fisher, Daniel G. Murri, Wendy R. Lanser
Dryden Flight Research Center
Edwards, California

National Aeronautics and
Space Administration

Office of Management

Scientific and Technical
Information Program

1996

EFFECT OF ACTUATED FOREBODY STRAKES ON THE FOREBODY AERODYNAMICS OF THE NASA F-18 HARV

David F. Fisher
NASA Dryden Flight Research Center
Edwards, CA

Daniel G. Murri
NASA Langley Research Center
Hampton, VA

Wendy R. Lanser
NASA Ames Research Center
Moffett Field, CA

ABSTRACT

Extensive pressure measurements and off-surface flow visualization were obtained on the forebody and strakes of the NASA F-18 High Alpha Research Vehicle (HARV) equipped with actuated forebody strakes. Forebody yawing moments were obtained by integrating the circumferential pressures on the forebody and strakes. Results show that large yawing moments can be generated with forebody strakes. At angles of attack greater than 40°, deflecting one strake at a time resulted in a forebody yawing moment control reversal for small strake deflection angles. At α = 40° and 50°, deflecting the strakes differentially about a 20° symmetric strake deployment eliminated the control reversal and produced a near linear variation of forebody yawing moment with differential strake deflection. At α = 50° and for 0° and 20° symmetric strake deployments, a larger forebody yawing moment was generated by the forward fuselage (between the radome and the apex of the leading-edge extensions), than on the radome where the actuated forebody strakes were located. Cutouts on the flight vehicle strakes that were not on the wind tunnel models are believed to be responsible for deficits in the suction peaks on the flight radome pressure distributions and differences in the forebody yawing moments.

NOMENCLATURE

ANSER	actuated nose strakes for enhanced rolling
C_{n0}	aircraft yawing moment at β = 0°
$C_{n0,\,fb}$	forebody (F.S. = 60 to 190) yawing moment at β = 0° from integrated pressures
$C_{n0,\,ff}$	forward fuselage (F.S. = 124.5 to 190) yawing moment at β = 0° from integrated pressures

$C_{n0,\,rad}$	radome (F.S. = 60 to 124.5) yawing moment at $\beta = 0°$ from integrated pressures
C_p	pressure coefficient, $(p - p_0)/q_\infty$
CFD	computational fluid dynamics
F.S.	fuselage station, in.
h_p	pressure altitude, ft
HARV	High Alpha Research Vehicle
HATP	High-Alpha Technology Program
M	Mach number
p	local pressure, lb/ft^2
p_0	free-stream static pressure, lb/ft^2
q_∞	free-stream dynamic pressure, lb/ft^2
Re_c	Reynolds number based on mean aerodynamic chord of 11.525 ft
y/b	strake span location divided by the local strake span
α	aircraft angle of attack, deg, from left wingtip angle-of-attack vane corrected for upwash and boom bending
β	aircraft angle of sideslip, deg, average of left- and right-wingtip sideslip vanes corrected for angle of attack, deg
$\Delta C_{n\,-30°rud}$	incremental change in aircraft yawing moment coefficient due to a –30° deflection of both rudders
δ_s	single strake deflection, deg
$\delta_{s,d}$	differential strake deflection, right strake deflection minus left strake deflection, deg
$\delta_{s,\,L/R}$	left and right strake deflection measured from the retracted position, deg
θ	forebody cross-section circumferential angle, deg (0° is bottom centerline, positive is clockwise as seen from a front view, 0° to 360°)

INTRODUCTION

The NASA High-Alpha Technology Program (HATP) was initiated to increase understanding, improve prediction techniques, provide design guidelines, and investigate new concepts for controls effectors on advanced, highly maneuverable aircraft at high angles of attack.[1] This program uses the F-18 configuration as a validation and demonstration vehicle. The flight vehicle consists of a highly modified F-18 referred to as the High Alpha Research Vehicle (HARV).[2] The HATP consists of wind-tunnel tests of subscale and full-scale models and components, calibration for computational fluid dynamics codes, piloted simulations, and full-scale flight testing. New ground

test, computational fluid dynamics, and flight test results have been obtained and techniques have been developed as a result of this program. These results and techniques have been summarized in three high angle-of-attack conference publications.[3–5]

Several new concepts for control at high angles of attack have been investigated in the wind tunnel and with computational fluid dynamics. Such concepts include engine thrust vectoring[6] and forebody vortex control using actuated forebody strakes[7,8] and pneumatic blowing.[9,10] An in-flight closed-loop thrust-vectoring system has been installed on the HARV, and the results have been documented.[11] Recently, closed-loop actuated forebody strakes have been installed, and preliminary results are reported in the present high-angle-of-attack conference. Although not a part of HATP, an open-loop pneumatic blowing flight control system was flight-tested on the X-29A airplane at high angles of attack.[12,13]

This paper examines the local flow aerodynamics of the forebody strakes and their effect on the forebody aerodynamics of the aircraft. Local forebody pressure distributions and forebody yawing moment results obtained on the F-18 HARV during the Actuated Nose Strakes for Enhanced Rolling (ANSER) program are presented. The ANSER acronym refers to “rolling” because the strakes provide the critical yaw control required to coordinate rolling maneuvers about the velocity vector at high angle-of-attack conditions.[14,15] Forebody yawing moments are presented for maximum single strake deployments for α = 20°–65°. Forebody yawing moments are also presented for four symmetric strake deployments for α = 30°, 40°, 50°, and 60°. Pressure distributions are presented at α = 50° for two symmetric strake deployments. Comparisons with ground facility results for a full-scale F-18 model are included.

EXPERIMENT DESCRIPTION

The following description of the vehicle and instrumentation used in this experiment supplied the basis for data collected.

Vehicle Description

Figure 1 shows the F-18 HARV. This highly modified full-scale development twin-engine, single-place, fighter/attack (F/A) airplane was originally built for the U.S. Navy by the McDonnell Douglas Corporation (St. Louis, Missouri) and the Northrop Corporation (Newbury Park, California). The F-18 HARV is powered by two modified General Electric (Lynn, Massachusetts) F404-GE-400 afterburning turbofan engines rated at approximately 16,000 lbf static thrust at sea level.

The F-18 HARV features a midwing configuration with a wing-root leading-edge extension that extends from the forward portion of the fuselage and blends into the wing. The F-18 HARV carries no stores or missiles and is highly instrumented for research purposes. The wingtip launching rails and missiles were replaced with specially designed camera pods and airdata sensors.[16] More specific details of the F-18 HARV can be found in reference 2.

EC96 43540-29

Figure 1. F-18 HARV aircraft with ANSER radome, $\alpha \approx 30°$, $\delta_{s,\,L/R} = 0°/90°$.

The HARV was modified by adding externally mounted engine thrust vanes for the deflection of the exhaust to provide additional pitching and yawing moments. The engines were modified to accommodate the thrust-vectoring vane installation by removing the divergent flap portion of the nozzle. The thrust-vectoring capability was provided by controlled deflection of the vanes (three for each engine), which moved into the engine exhaust plume (ref. 2).

For the ANSER program, a new radome was fabricated at NASA Langley Research Center (LaRC), Hampton, Virginia, that incorporated hydraulically operated conformal actuated forebody strakes. Figure 2 shows a schematic of the strakes. These strakes are 48 in. long and are positioned longitudinally 120° up from the bottom of the forebody beginning at 8 in. aft of the forebody apex.

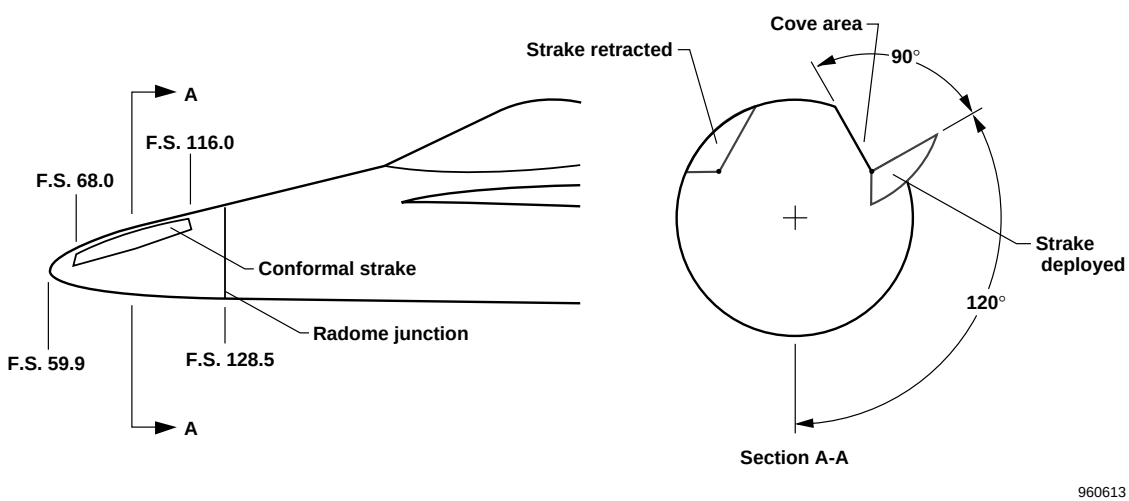

Figure 2. Sketch of forebody strakes on the F-18 HARV.

Figure 3 shows a closeup photograph of the left strake. When the strakes are closed, there are no protrusions, and the external mold line of the radome conforms to the original radome shape. Figures 4(a) and 4(b) show the airplane with the right strake (pilot view) deployed at 30° and 90° respectively.

Instrumentation

The fuselage forward of the cockpit was extensively instrumented with surface pressure measurements (fig. 5). Five circumferential rings of pressure orifices were installed on the surface of the radome and forward fuselage, forward of the cockpit canopy at fuselage station (F.S.) 70, F.S. 85, F.S. 107, F.S. 142, and F.S. 184. On each forebody strake, three rows of orifices were installed on the outboard surface at F.S. 70, F.S. 85, and F.S. 107, and two on the inboard surface at F.S. 85 and F.S. 107. In addition, three rows of orifices (F.S. 70, F.S. 85, and F.S. 107) were installed on the cove section of the forebody. This region of the forebody is exposed when the strake is actuated. The forebody pressures were measured with a ±216 lbf/ft^2 differential pressure transducer, and the strakes used ±720 lbf/ft^2 transducers. The accuracy was estimated to be ±1 lbf/ft^2 for the forebody pressures and ±3 lbf/ft^2 for the strake pressures. More detailed information of the instrumentation has been given previously.[17]

Airspeed, altitude, angle of attack (α) and angle of sideslip (β) were measured using airspeed booms mounted on specially designed wingtip photograph pods. A swiveling probe that was designed with four vanes to align the pitot-static probe head with the local airstream was on the left wingtip.[16] Aircraft angle of attack was measured by using a vane on the right wingboom and

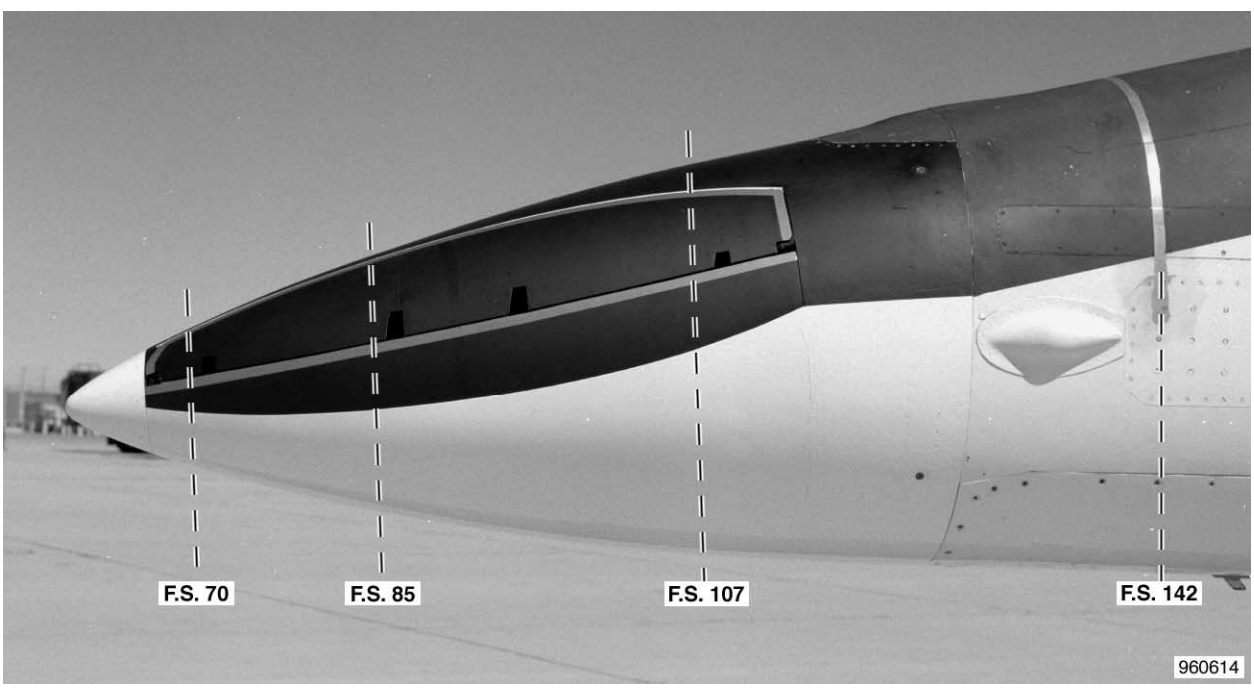

Figure 3. Close-up photo of left forebody strake.

EC96 43598-9

(a) $\delta_{s,\ L/R} = 0°/30°$.

Figure 4. F-18 HARV with ANSER radome and right forebody strake deployed.

(b) $\delta_{s,\ L/R} = 0°/90°$.

Figure 4. Concluded.

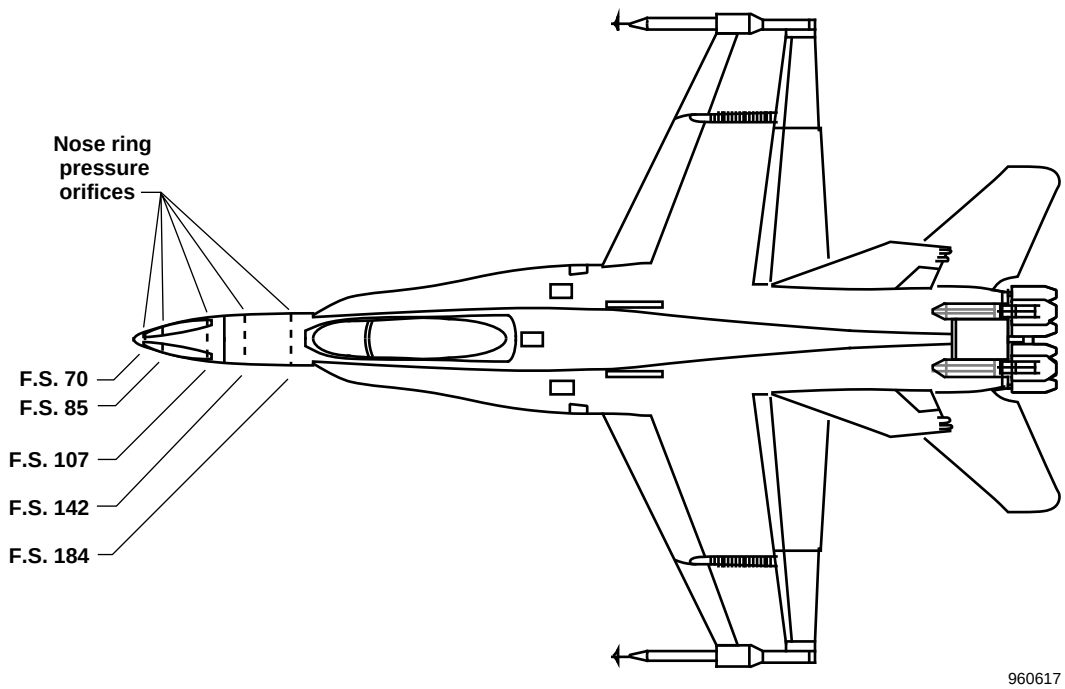

Figure 5. Location of pressure orifices on F-18 HARV forebody.

corrected for upwash and boom bending. Angle of sideslip was determined as the average of the left- and right-wingboom sideslip vane measurement corrected for angle of attack.

Data from these measurements, as well as from the standard aircraft control positions, inertial systems, and accelerometer parameters, were transmitted to a ground station. These critical parameters were monitored by engineers and technicians in real time on strip charts and displays. These data were monitored in near real time at NASA Dryden Flight Research Center, Edwards, California, and Langley Research Center, Hampton, Virginia.

On selected flights, smoke flow visualization was used to mark and identify the off-surface forebody/strake vortical flows. For these flights, the nose cap on the ANSER radome was replaced with one that had two 1.0 in. diameter smoke ports, placed symmetrically 60° up from the bottom centerline. Figure 6 shows a closeup of the right smoke port and radome after a flight. White smoke from a smoke generator system[18] used previously[19] on the F-18 HARV was fed from the smoke generator system through a single 1.5–in. diameter tube to the two 1.0–in. diameter symmetrically located ports on the nose cap. Also shown in figure 6 are six cutouts on the lower portion of the right strake that provided clearance for the radome bulkheads. These cutouts will be discussed later in Results and Discussion.

DATA REDUCTION TECHNIQUES

For the forebody and strake pressures, in-flight zero differential pressures were taken before each test point and were used in postflight data reduction to correct the data for calibration offsets.

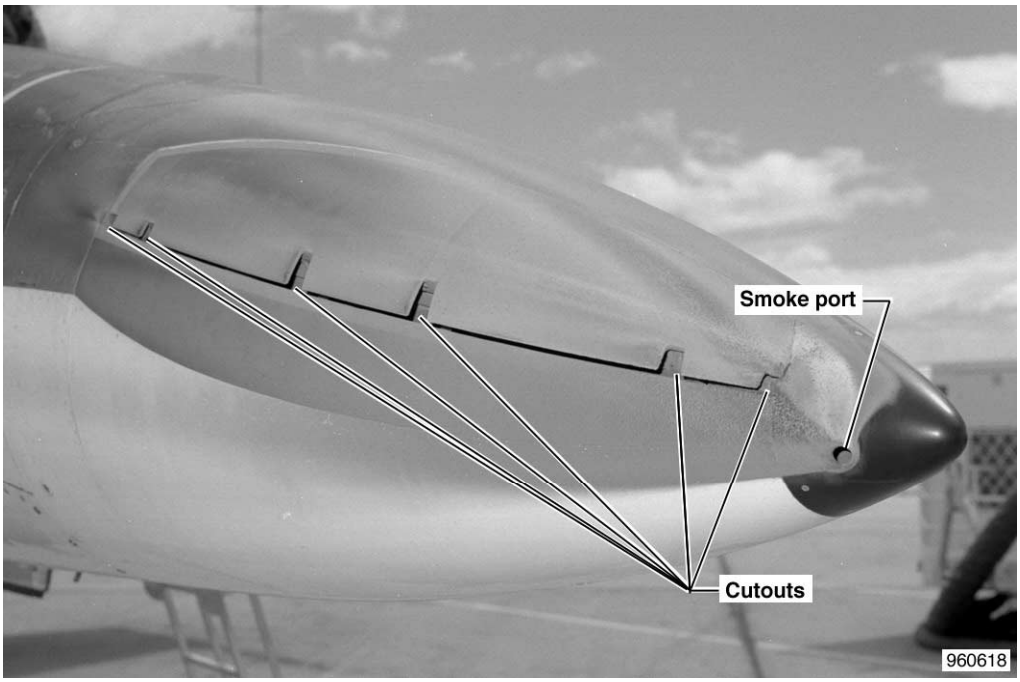

Figure 6. Close-up of right smoke port and strake cutouts on ANSER radome.

Time segments of 1.0 sec duration were used for data analysis purposes with approximately 25 time points averaged.

Forebody yawing moment coefficients were determined by integrating the five rings of pressures on the forebody, the pressures on the coves, and the pressures on the strakes over their respective projected forebody side areas. For the forebody, this area extended from the forebody apex to the apex of the wing leading-edge extensions. Pressures were integrated for flight conditions in which the angle of sideslip was less than ±0.5° to determine the yawing moment at 0° sideslip.

During data analysis, pressure coefficients were noted on the lower fuselage centerline that were greater than 1.0 during extremely high-angle-of-attack flight, $\alpha \geq 60°$. This anomaly had not been noted in earlier flight tests.[17,20] At these angles of attack, the aircraft is no longer able to maintain constant altitude. In fact, the aircraft descended at a rate of 200–300 ft/sec. During subsequent hangar tests of the swiveling probe pitot- and static-pressure orifices, an approximate 0.3-sec lag was noted. Possibly, the flexible pressure tubing for the swiveling probe pitot and static pressures had become restricted as compared to previous flight data. For the flight conditions of the data within this paper, ($M \leq 0.4$ and altitudes near 25,000 ft), this lag was estimated to be approximately 0.6 sec after adjusting for the change in density and viscosity at altitude.[21] Therefore, for these results, the pitot static data were time skewed by 0.6 sec.

FLIGHT TEST CONDITIONS

Data were obtained in quasi-stabilized 1-*g* flight maneuvers at a nominal altitude of 25,000 ft and $M \leq 0.4$ for $\alpha = 20°–65°$. At angles of attack greater than approximately 30°, constant altitude

could not be maintained, and these data were obtained in a descent. The pressure distribution data were obtained during open-loop flight maneuvers, and the flow visualization data were obtained during open- and closed-loop maneuvers. For the data presented, with few exceptions, $|\beta| \leq 0.5°$. Table 1 lists the test points and flight conditions.

Table 1. Flight conditions for HARV ANSER pressure distribution test points.

Test point	α, deg	β, deg	M	Re_c E–6	q_∞	h_p	δ_s, right	δ_s, left	$\delta_{s,d}$	$C_{n0,\ fb}$	C_{n0}, rad	$C_{n0,\ ff}$
flt0336.nz.02	20	0	0.328	12.2	59.4	24886	–0.3	89.6	–89.9	0.0033	0.0020	0.0013
flt0336.nz.04	20	–0.1	0.35	13.07	67.7	24923	89.6	–0.3	89.9	–0.0032	–0.0018	–0.0014
flt0333.nz.02	24.6	0.3	0.303	12.73	58.6	21545	–0.2	89.7	–89.9	0.0059	0.0032	0.0027
flt0343.nz.08	25.1	0	0.335	12.42	61.4	25070	–0.5	–0.5	–0.1	0.0001	0.0002	–0.0001
flt0333.nz.06	25	0.8	0.27	11.68	47.9	20073	89.6	–0.2	89.8	–0.0068	–0.0033	–0.0034
flt0333.nz.01	29.6	0	0.288	11.79	51.1	22302	–0.2	89.7	–89.8	0.0108	0.0049	0.0058
flt0343.nz.07	30	0.3	0.273	9.52	37.3	27162	–0.5	59.7	–60.2	0.0084	0.0037	0.0048
flt0333.nz.05	29.7	0.5	0.288	12.07	52.7	21634	–0.3	29.7	–29.9	0.0033	0.0012	0.0021
flt0336.nz.11	30.2	0.2	0.259	10.46	41	22598	–0.3	19.7	–20	0.0015	0.0006	0.0009
flt0352.nz.03	32.6	0.2	0.27	10.24	40.1	24915	4.6	14.7	–10.1	0.0007	0.0001	0.0005
flt0336.nz.01	30.1	0.1	0.294	10.8	46.7	25345	–0.2	9.7	–9.9	0.0001	0.0003	–0.0002
flt0335.nz.12	29.8	0.1	0.294	11.23	47	25306	–0.6	–0.6	0	0.0003	0.0003	0.0000
flt0352.nz.02	30.2	0	0.309	12	54	24402	9.7	9.7	0	0.0000	0.0001	0.0000
flt0336.nz.03	30.2	0	0.323	11.42	53.4	26631	9.7	–0.2	10	–0.0005	0.0000	–0.0004
flt0352.nz.04	32.3	0.1	0.252	9.87	36.7	23926	14.7	4.6	10.1	–0.0009	–0.0001	–0.0008
flt0336.nz.13	29.9	0.1	0.273	10.84	44.5	23027	19.7	–0.4	20.1	–0.0019	–0.0004	–0.0016
flt0336.nz.06	29.8	–0.2	0.304	10.95	48.5	26077	29.7	–0.3	30	–0.0034	–0.0009	–0.0026
flt0336.nz.07	30.3	0.1	0.328	11.56	54.7	26801	59.7	–0.3	60	–0.0083	–0.0032	–0.0051
flt0336.nz.08	29.8	–0.2	0.297	11.24	49.3	24625	89.6	–0.3	90	–0.0103	–0.0044	–0.0059
flt0335.nz.02	35.1	–0.2	0.307	10.4	42.6	29380	–0.2	89.6	–89.9	0.0162	0.0070	0.0092
flt0335.nz.03	35.1	–0.1	0.301	10.65	43.8	27904	–0.2	–0.2	0	0.0003	0.0003	0.0000
flt0336.nz.09	35.2	–0.2	0.259	10.42	40.6	22809	89.6	–0.3	90	–0.0156	–0.0063	–0.0094
flt0335.nz.21	39.9	0	0.27	10.18	38.4	25903	–0.6	89.6	–90.2	0.0218	0.0093	0.0125
flt0334.nz.02	40	0.1	0.279	10.42	41.3	25779	–0.2	59.7	–59.9	0.0173	0.0062	0.0111
flt0337.nz.09	40.6	0.3	0.24	9.72	34.9	22739	4.6	34.7	–30	0.0090	0.0022	0.0068
flt0334.nz.06	39.3	–0.4	0.284	10.03	39.6	27582	–0.3	29.6	–29.9	0.0056	0.0016	0.0039
flt0337.nz.03	39.9	0	0.278	9.92	39.5	26615	9.7	29.7	–19.9	0.0070	0.0018	0.0052
flt0351.nz.01	40	0.3	0.29	10.18	39.8	28398	–0.2	19.7	–19.9	0.0000	0.0002	–0.0002
flt0352.nz.05	39.2	–0.3	0.268	10.05	38.7	25372	4.6	14.7	–10.1	0.0001	0.0001	0.0000
flt0336.nz.10	40.6	–0.1	0.258	9.76	37.3	24617	–0.3	9.7	–9.9	–0.0023	0.0000	–0.0022
flt0338.nz.02	39.7	–0.1	0.29	10.5	43.5	26332	14.7	24.7	–9.9	0.0035	0.0007	0.0028
flt0338.nz.03	39.8	–0.1	0.271	10.21	40.1	25133	–0.2	–0.2	0	0.0005	0.0005	0.0000
flt0352.nz.01	40	–0.1	0.272	9.64	36.9	27192	9.7	9.7	0	0.0010	0.0004	0.0006
flt0337.nz.13	40	0.2	0.241	9.8	35.5	22531	19.7	19.7	0.1	0.0000	0.0002	–0.0001
flt0338.nz.05	39.6	–0.1	0.3	10.44	43.9	27746	24.7	14.7	10	–0.0032	–0.0003	–0.0028
flt0336.nz.12	39.9	–0.1	0.273	10.21	41.3	24907	9.7	–0.4	10.1	0.0019	0.0007	0.0012
flt0352.nz.06	39.6	–0.1	0.263	10.02	38.1	25038	14.7	4.5	10.2	0.0011	0.0006	0.0006
flt0333.nz.10	40	0.1	0.201	8.87	27.4	20163	19.7	–0.3	20	–0.0009	0.0004	–0.0013

Table 1. Continued.

Test point	α, deg	β, deg	M	Re_c E–6	q_∞	h_p	δ_s, right	δ_s, left	$\delta_{s,d}$	$C_{n0,\ fb}$	C_{n0}, rad	$C_{n0,\ ff}$
flt0334.nz.07	40.4	0	0.255	9.73	35.7	25100	29.7	–0.2	29.9	–0.0059	–0.0007	–0.0051
flt0337.nz.06	40.3	0.1	0.256	10.09	38.4	23469	34.7	4.5	30.2	–0.009	–0.0021	–0.0069
flt0334.nz.04	40	–0.1	0.285	9.9	38.9	28168	59.7	–0.2	59.9	–0.0171	–0.0053	–0.0118
flt0338.nz.06	39.8	0.1	0.277	9.93	39.6	26449	89.6	–0.3	89.9	–0.0197	–0.0068	–0.0129
flt0335.nz.25	44.8	0.1	0.301	10.12	40.3	29833	–0.6	89.7	–90.2	0.0297	0.0122	0.0175
flt0337.nz.05	44.9	0	0.265	9.86	37.9	25413	–0.1	–0.1	0	0.0000	0.0003	–0.0002
flt0335.nz.27	44.5	0.3	0.313	11.2	47.4	27928	89.6	–0.5	90.2	–0.0286	–0.0106	–0.0180
flt0336.nz.14	50.2	–0.2	0.262	9.32	35.5	26365	–0.3	89.6	–90	0.0337	0.0149	0.0187
flt0335.nz.19	50	0.2	0.243	10.12	36.6	22142	–0.6	59.7	–60.3	0.0241	0.0093	0.0148
flt0337.nz.08	49.5	0.2	0.253	9.66	35.5	24830	4.6	34.7	–30	0.0127	0.0024	0.0103
flt0337.nz.07	49.8	–0.1	0.315	9.35	38.9	32539	–0.2	29.7	–29.8	0.0017	0.0006	0.0011
flt0343.nz.04	49.7	–0.1	0.276	9.97	39.7	26274	9.7	29.7	–20	0.0076	0.0015	0.0061
flt0352.nz.09	48	0.2	0.261	9.84	36.6	25529	19.7	39.6	–19.9	0.0152	0.0043	0.0110
flt0351.nz.02	49.8	0.1	0.257	10.56	38.5	23680	–0.1	19.7	–19.9	–0.0091	–0.0012	–0.0079
flt0352.nz.07	49.3	–0.3	0.263	9.39	34.6	27206	24.7	34.7	–10	0.0111	0.0025	0.0086
flt0335.nz.16	49.7	0.1	0.296	10.38	41.9	28185	14.7	24.7	–10	0.0035	0.0007	0.0028
flt0338.nz.01	50.1	0	0.292	9.07	35.3	31342	14.7	24.7	–9.9	0.0028	0.0007	0.0022
flt0333.nx.01	49.9	–0.1	0.248	10.04	37	22878	–0.2	9.7	–9.9	–0.0081	–0.0011	–0.0070
flt0337.nz.11	49.8	0.2	0.271	9.24	34.9	28272	–0.3	–0.2	–0.1	0.0001	0.0002	–0.0001
flt0357.nz.03	50.9	0.2	0.241	9.29	31.3	25523	29.7	29.6	0	–0.0010	–0.0001	–0.0009
flt0335.nz.17	50	0.3	0.256	10.18	37.3	24288	19.7	19.7	0	0.0017	0.0002	0.0015
flt0333.nx.02	49.7	–0.2	0.241	9.94	36	22205	9.7	–0.2	9.9	0.0084	0.0019	0.0065
flt0352.nz.08	48.7	–0.7	0.24	9.56	32.9	23253	34.7	24.7	10	–0.0095	–0.0018	–0.0077
flt0335.nz.18	49.8	–0.2	0.237	10.11	35.9	21429	24.7	14.7	10	–0.0035	–0.0006	–0.0029
flt0352.nz.10	50.2	–0.4	0.227	9.45	31.6	22374	39.7	19.7	20	–0.0162	–0.0043	–0.0119
flt0335.nz.23	50	0	0.279	10.19	38.7	27274	29.7	9.7	20	–0.0074	–0.0014	–0.0060
flt0339.nz.06	49.7	0.2	0.257	9.74	36.5	24929	19.7	–0.3	20.1	0.0082	0.0019	0.0063
flt0357.nz.02	47.2	–0.4	0.235	10.81	38.2	19568	44.7	14.7	30	–0.0184	–0.0051	–0.0133
flt0335.nz.29	50.1	0	0.248	10.19	36.8	23057	34.7	4.6	30.1	–0.0127	–0.0023	–0.0104
flt0335.nz.15	49.3	0	0.265	10.88	42.4	22879	29.7	–0.6	30.2	–0.0040	–0.0005	–0.0035
flt0337.nz.12	50.1	0.1	0.257	9.32	34.2	26369	59.7	–0.2	60	–0.0264	–0.0092	–0.0172
flt0336.nz.15	50.2	0.1	0.242	9.4	33.9	23909	89.7	–0.4	90	–0.0345	–0.0138	–0.0207
flt0341.nz.09	55.1	–0.4	0.257	9.67	36	25255	–0.2	89.7	–89.9	0.0368	0.0180	0.0189
flt0341.nz.07	55.2	0	0.25	8.87	31.8	26772	–0.2	–0.2	0	–0.0002	0.0002	–0.0004
flt0341.nz.10	55.1	0.4	0.233	9.59	33.3	22367	89.6	–0.2	89.8	–0.0379	–0.0170	–0.0209
flt0342.nz.06	59.8	–0.1	0.276	11.07	45.8	22850	–0.5	89.7	–90.2	0.0356	0.0210	0.0146
flt0342.nz.04	59.7	0.4	0.287	11.22	47.5	23839	–0.5	59.7	–60.2	0.0203	0.0121	0.0082
flt0375.nz.07	58.2	–0.2	0.267	10.22	40.8	24087	14.7	44.7	–29.9	0.0247	0.0087	0.0160
flt0342.nz.01	60.8	0.1	0.271	11.05	45.3	22288	–0.3	19.7	–20	–0.0112	–0.0068	–0.0044
flt0375.nz.14	60.4	0.2	0.282	9.37	37.7	28348	19.7	39.6	–19.9	0.0219	0.0080	0.0139
flt0343.nz.05	59.9	0.4	0.298	10.35	43.9	27434	–0.5	9.7	–10.1	–0.0084	–0.0014	–0.0070
flt0358.nz.01	60.2	0.2	0.284	11.4	45.1	24594	24.7	34.7	–10	0.0210	0.0058	0.0153
flt0357.nz.04	59.1	0.1	0.23	9.9	33	21994	29.7	29.6	0	0.0087	0.0015	0.0072
flt0358.nz.02	59.8	0.3	0.264	10.76	40.4	23821	34.7	24.7	10	–0.0120	–0.0025	–0.0095

Table 1. Concluded.

Test point	α, deg	β, deg	M	Re_c E–6	q_∞	h_p	δ_s, right	δ_s, left	$\delta_{s,d}$	$C_{n0,\ fb}$	C_{n0}, rad	$C_{n0,\ ff}$
flt0343.nz.06	59.9	–0.3	0.284	11.04	46.2	24118	9.7	–0.5	10.2	0.0173	0.0061	0.0112
flt0342.nz.02	59.3	0.5	0.248	8.76	31.6	26531	19.2	–0.3	19.5	0.0191	0.0080	0.0111
flt0375.nz.05	59.9	–0.2	0.284	10.47	43.7	25235	39.7	19.7	20	–0.0154	–0.0061	–0.0093
flt0342.nz.03	59.7	0.2	0.266	9.35	36.2	26704	29.7	–0.3	30	0.0132	0.0053	0.0079
flt0342.nz.05	59.6	0.4	0.288	11.11	47.1	24213	59.7	–0.5	60.2	–0.0182	–0.0105	–0.0076
flt0342.nz.07	60.1	0.5	0.28	10.29	42.6	25871	89.6	–0.4	90	–0.0309	–0.0192	–0.0117
flt0342.nz.09	64.6	0.7	0.3	11.1	48	24933	–0.5	89.7	–90.1	0.0291	0.0222	0.0069
flt0343.nz.02	64.5	1.7	0.28	10.5	41.5	26253	–0.3	–0.3	0	–0.0003	0.0010	–0.0013
flt0342.nz.10	64.9	1.1	0.27	11.22	45.6	22214	89.6	–0.4	90	–0.0260	–0.0206	–0.0053

RESULTS AND DISCUSSION

This section first discusses the forebody yawing moments to show the overall effect of the forebody strakes. The forebody and strake pressure distributions are then discussed to explain causes for some forebody yawing moment results. Flow visualization is used to support the interpretation of the pressure distributions. Finally, pressure distributions from a full-scale wind tunnel model are presented for comparison.

Forebody Yawing Moments

Figure 7 shows the yawing moment at 0° sideslip from the 30- by 60-Ft[22] and 80- by 120-Ft[23] Wind Tunnels for the complete airplane are presented as a function of angle of attack for left and

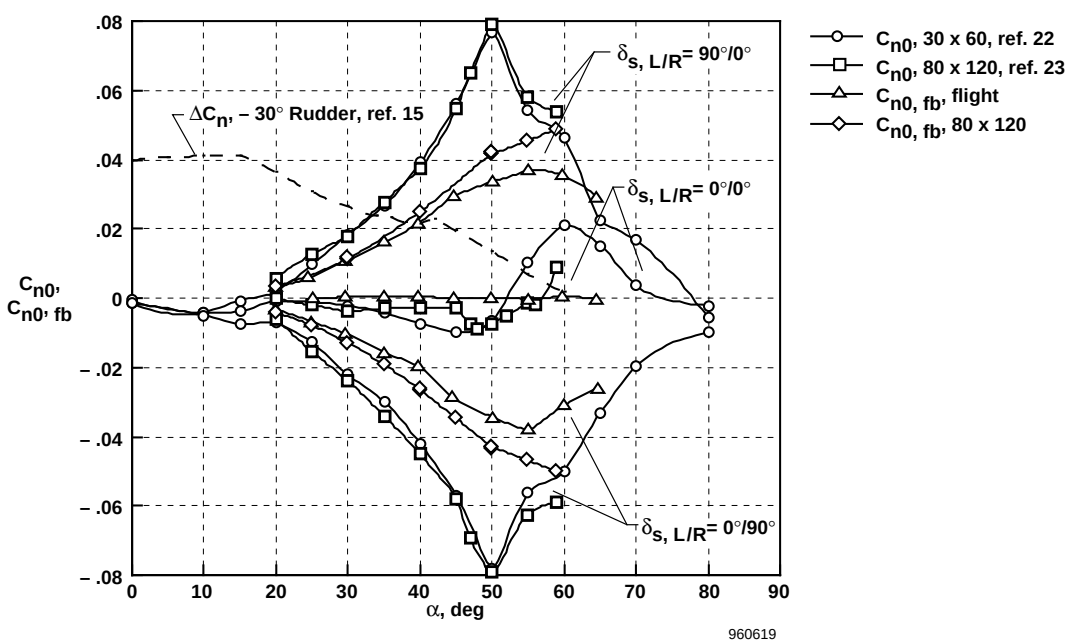

Figure 7. Comparison of forebody yawing moments from flight and wind tunnel and total aircraft yawing moments from wind tunnel.

right strake deflections, $\delta_{s,\,L/R}$ = 90°/0°, 0°/0°, and 0°/90°. Figure 7 also shows yawing moments for just the forebody alone (F.S. 60 to F.S. 190) from flight and the 80- by 120-Ft Wind Tunnel. Note that when the left strake is deflected, 90°/0°, the yawing moment is positive or to the right and the converse is true when the right strake is deflected, 0°/90°. This same figure shows the strong effectiveness of the actuated forebody strakes at high angle of attack, especially when compared to the rudder. The maximum forebody yawing moment from flight is approximately one-half of the total maximum aircraft yawing moment from the wind tunnels. At α = 50° the flight forebody yawing moment is approximately 80 percent of the wind-tunnel value. The peak forebody yawing moment from flight was at α = 55° and at α = 59° (maximum test α) for the wind tunnel. For the whole airplane, the maximum yawing rate was at α = 50°. At α = 59° for the wind tunnel and α = 65° for flight, the forebody and total aircraft yawing moments were approximately equivalent. The differences between the flight and wind-tunnel forebody yawing moments will be discussed further in the Pressure Distributions subsection.

During development in wind-tunnel tests,[15] deflecting one strake at a time at high angles of attack could result in a small but undesirable control reversal at small strake deflections. To overcome this undesirable characteristic for closed-loop control, a solution was developed that deploys the strakes symmetrically as angle of attack increases to α = 30° and greater. When a yawing moment is desired under these conditions, the strakes are deflected differentially about a symmetric strake deployment (fig. 8). For example, using the 20° symmetric strake schedule, (fig. 8(c)), $\delta_{s,d}$ = 0° would correspond to $\delta_{s,\,L/R}$ = 20°/20°, $\delta_{s,d}$ = 10° would correspond to $\delta_{s,\,L/R}$ = 15°/25°, $\delta_{s,d}$ = 20° would correspond to $\delta_{s,\,L/R}$ = 10°/30° and so on. For all angles of attack, however, the maximum yaw control deflection would always consist of one strake fully deployed (90°) and the other strake fully retracted (0°).

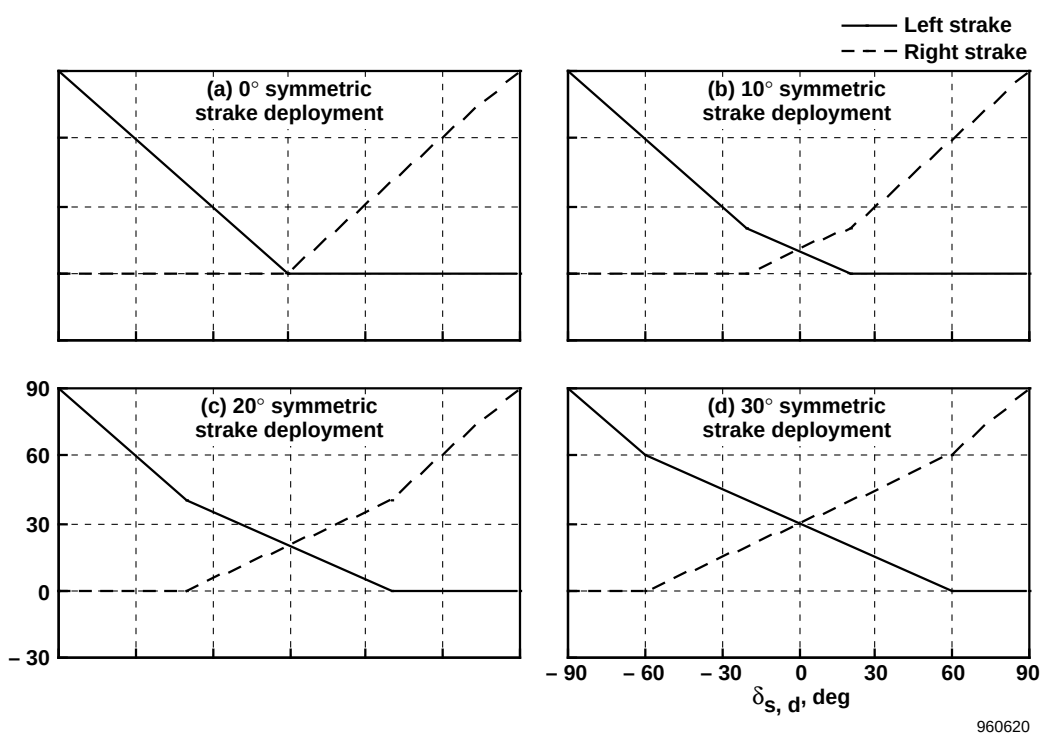

Figure 8. Symmetric strake deployment schedules.

Figure 9 shows the forebody yawing moments from flight as a function of differential strake deflection, $\delta_{s,d}$, (right strake deflection minus the left strake deflection). At α = 30°, these data show the variation of forebody yawing moment with differential strake deflection for the 0° and 10° symmetric strake deployments (fig. 9(a)). For the 0° symmetric strake deployment, the left and right strakes are at 0° (closed) when no yawing moment is desired. For the 10° symmetric strake deployment, the left and right strakes are deployed symmetrically to 10° when no yawing moment is desired. Very little difference is noted between the 0° and 10° symmetric strake deployments.

At α = 40°, data for the 0° symmetric strake deployment show a control reversal at $\delta_{s,d} = \pm 10°$ (fig. 9(b)). In this case as the strakes begin to open, the yawing moment is opposite to the desired direction. Data for the 10° symmetric strake deployment are better but still show a slight reversal. In this case at α = 40°, the 20° symmetric strake deployment eliminates the control reversal and results in a nearly linear variation of forebody yawing moment.

At α = 50°, a similar trend is seen (fig. 9(c)). The 0° symmetric strake deployment results in a large control reversal. As at α = 40°, the 20° symmetric deployment eliminates the control reversal and results in a nearly linear variation of forebody yawing moment for differential strake deflections. The 30° symmetric strake deployment also eliminates the control reversal, but the curve does not have the desired linear slope.

At α = 60°, the control reversal in yawing moment for the 0° symmetric strake deployment becomes larger and asymmetric (fig. 9(d)). The forebody yawing moment at $\delta_{s,d}$ = 20° (0°/20°) is approximately double that at $\delta_{s,d}$ = –20° (20°/0°). The 30° symmetric strake deployment is an improvement but is not as linear as desired.

For comparison, figure 10 shows the forebody yawing moments at α = 50° for the 0° and 20° symmetric strake deployments from the 80- by 120-Ft Wind Tunnel. As compared with the flight forebody yawing moments, the yawing moment reversal for the 0° symmetric strake deployment from the wind tunnel is only about one-half the flight value (fig. 9(c)). The 20° symmetric strake deployment is much improved but not quite as linear as the flight case. The maximum forebody yawing rates from the wind tunnel at $\delta_{s,d} = \pm 90°$ is approximately 25 percent higher than the flight values. The explanation for these differences will be given later under the Pressure Distributions subsection.

In figure 11, the flight forebody yawing moments at α = 50° are broken down into two parts for the 0° and 20° symmetric strake deployments: the ANSER radome including strakes (F.S. = 60 to 124.5) and the forward fuselage between the radome and the apex of the wing leading-edge extension (F.S. = 124.5 to 190). For the 0° symmetric strake deployment, the majority of the yawing moment results from the side force on the forward fuselage, including the region of yawing moment reversal, $|\delta_{s,d}| < 30°$ (fig. 11(a)). Using the 20° symmetric strake deployment, the yawing moment reversal is no longer present for the radome and the forward fuselage (fig. 11(b)). Again, as for the 0° symmetric strake schedule, the strakes generate little yawing moment at $|\delta_{s,d}| < 30°$ as shown by the radome data. However, the vortices the strakes generate create a significant yawing moment further aft on the forward fuselage. Approximately 80 percent of the forebody yawing moment for $|\delta_{s,d}| \leq 30°$ at α = 50° is caused by the side forces on the forward fuselage. At $\delta_{s,d} = \pm 90°$ the forward fuselage accounts for 55–60 percent of the forebody yawing moment.

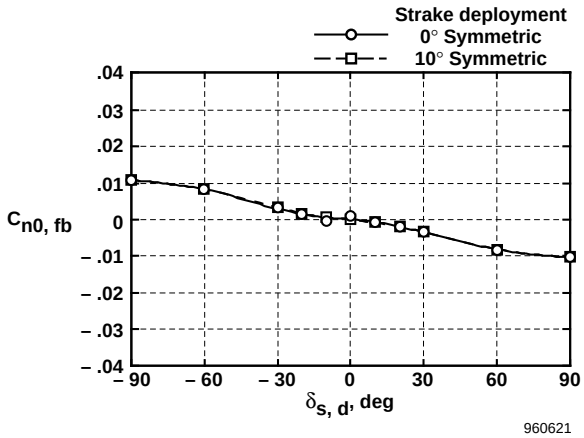

(a) $\alpha = 30°$.

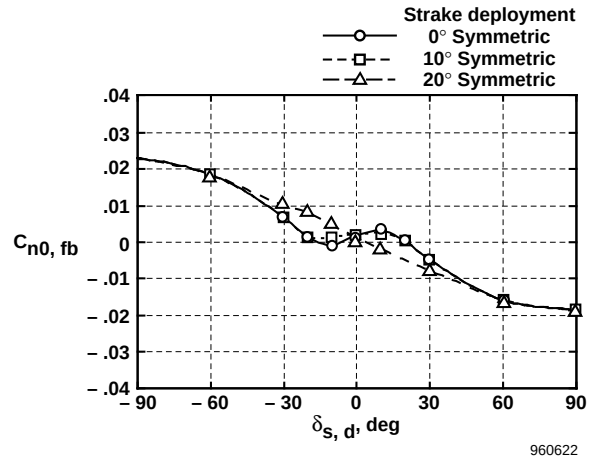

(b) $\alpha = 40°$.

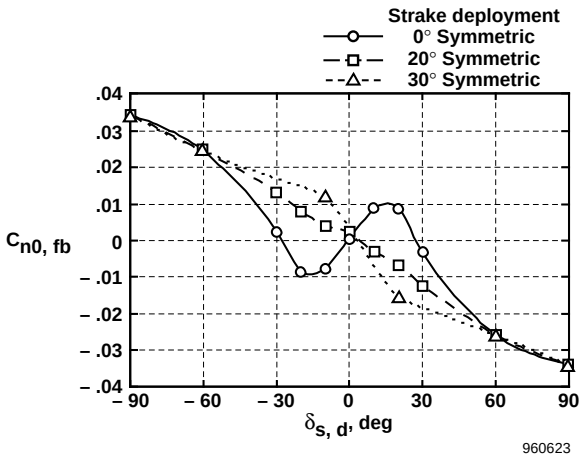

(c) $\alpha = 50°$.

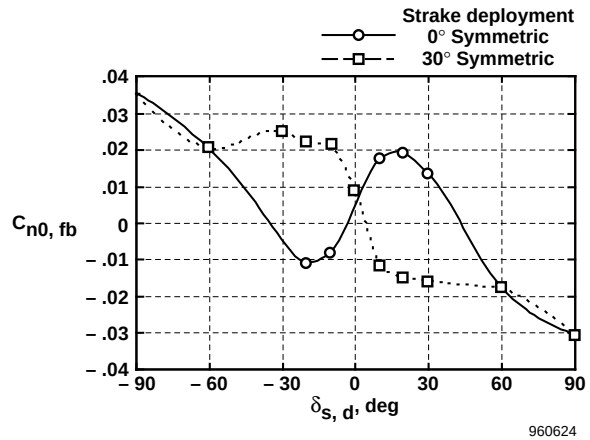

(d) $\alpha = 60°$.

Figure 9. Forebody yawing moments as a function of differential strake position, $\beta = 0°$.

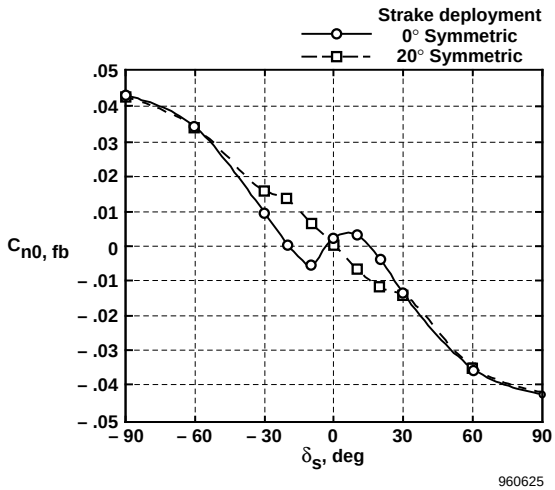

Figure 10. 80- by 120-Ft Wind Tunnel forebody yawing moments as a function of differential strake position, $\beta = 0°$, 0° and 20° symmetric strake deployments.

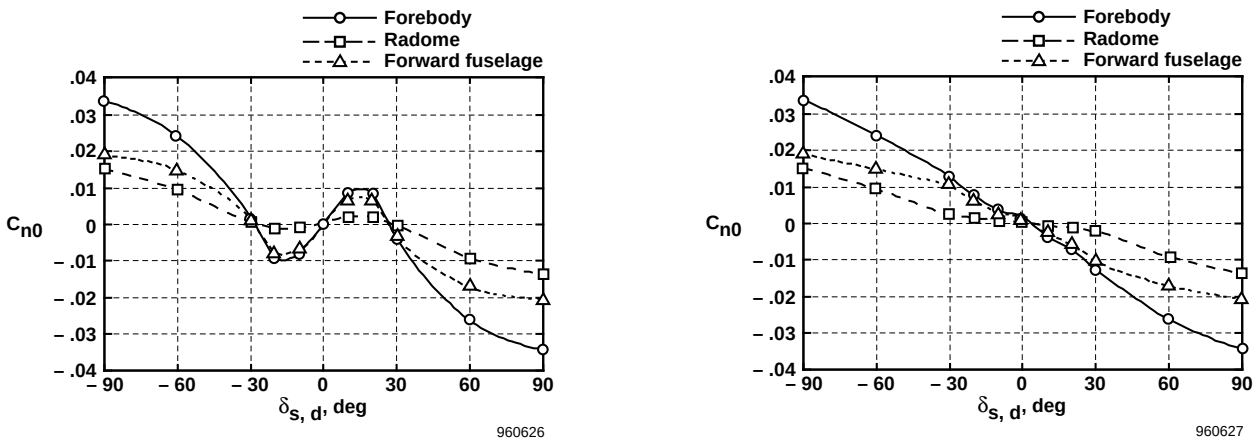

(a) 0° symmetric strake deployment.

(b) 20° symmetric strake deployment.

Figure 11. Forebody, radome, and forward fuselage yawing moments as a function of differential strake position, $\alpha = 50°$ and $\beta = 0°$.

Pressure Distributions

Figure 12 shows the forebody and deployed strake pressure distributions for $\alpha = 50°$ for the 0° and 20° symmetric strake deployments. This figure shows the aerodynamic mechanisms responsible for the yawing moments generated by the strakes. For the 0° symmetric strake deployment, large yawing moment reversals were present. For the 20° symmetric strake deployment, the yawing moments were linear. Separate plots are shown for the forebody and the right and left strakes. Note that the pressure distributions are offset by $C_p = 1.0$ for each consecutive fuselage station for clarity.

0° Symmetric Strake Deployment

Figure 12(a) shows the forebody pressure distributions as a function of the forebody cross-section circumferential angle, θ. The scale for the circumferential angle is reversed so that the pressure distributions can be viewed in the pilot's perspective. The $\theta = 0°$ and 360° are on the lower centerline; $\theta = 180°$ is on the top centerline; $\theta = 90°$ is on the right side of the fuselage; and $\theta = 270°$ is on the left. This convention was established in previous papers.[17,20] The symbols and solid curve indicate the pressure distribution from the HARV ANSER radome. The footprints of the forebody vortices can be seen by the suction peaks in the pressure distributions at $\theta \approx 160°$ and 200° for F.S. 85, F.S. 107, F.S. 142, and F.S. 184. The large suction peaks at $\theta \approx 90°$ and 270° for F.S. 70, F.S. 85, and F.S. 107 are caused by the acceleration of the flow around the fuselage that is nearly circular in cross-section. The small suction peak for F.S. 142 at $\theta \approx 110°$ and 250° is caused by a small antenna cover just forward of F.S. 142. The dashed curve indicates pressure distribution data obtained from the original HARV radome.[17] The most obvious difference between ANSER radome results and the original HARV radome results is the deficit in the suction peak at $\theta \approx 80°$ to 110° and 250° to 280°, starting at F.S. 70 and progressing aft to F.S. 107. The original HARV radome suction peak is much smoother and fuller. This deficit region is below the strake. The joint at $\theta \approx 280°$ (where the white and black paint meet below the strake) (fig. 3) could cause boundary-layer transition. Previously, however, boundary-layer trips very near this location on the original

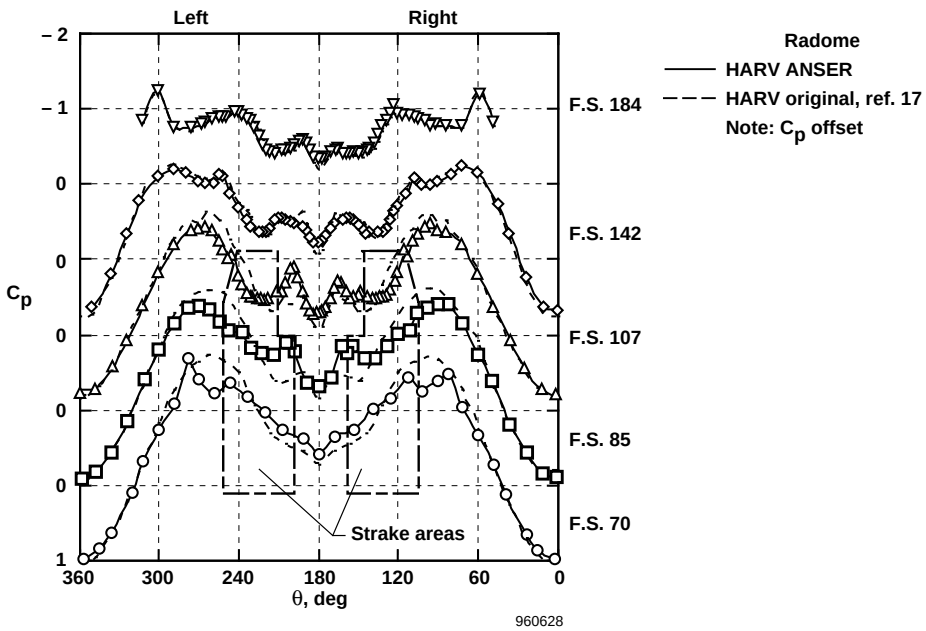

(a) $\delta_{s,\,L/R}$ = 0°/0° with comparison to previous flight results.

Figure 12. Forebody and strake pressure distributions with the ANSER radome at α = 50° for the 0° symmetric strake deployment, pilot's view.

HARV radome[24] did not show a deficit in this region but did show the enhanced vortex footprints at F.S. 85. The radome was checked for roundness in this region at F.S. 70 and F.S. 85, and the local curvature appeared to be satisfactory. The strakes were sealed from the interior of the radome and from top to bottom. The gap between the retracted strake and fuselage was on the order of 0.1 to 0.2 in. Large cutouts existed as shown previously in figure 6, some 1- by 1-in., and some 1.5- by 2-in. This deficit in the suction peak will be discussed further when the ANSER radome pressure distributions are correlated with the 80- by 120-Ft Wind-Tunnel model pressure distributions.

Figure 12(b) shows the pressure distributions at α = 50° for the right strake extended to 10°. At this strake deflection (fig. 9(c)), a strong yawing moment reversal with the yawing moment positive or to the right occurred. At this angle of attack, the footprints from forebody vortices that can be seen at θ ≈ 160° and 200° become asymmetric at F.S. 142 and F.S. 184. The pressure distribution on the right side, especially between θ ≈ 60° to 120°, tend to have lower pressures than on the left side at the same corresponding angles. This circumferential range of angles, θ ≈ 60° to 120° on the right side and the corresponding angles (240° to 300°) on the left side are important because they represent approximately 87 percent (sin 60°) of the forebody side area. At this strake deflection angle, the pressures on the outboard and inboard strake surfaces are below ambient ($C_p < 0$) with the outboard surface pressures less than the inboard surface pressures. Pressures on the forebody and the strake result in a yawing moment to the right, which was not the desired direction (figs. 9(c) and 11(a)).

With the right strake deflected 20°, the pressure distributions become more asymmetric with large suction peaks at θ ≈ 160° for F.S. 85 and F.S. 107 caused by the right forebody/strake vortex (fig. 12(c)). The right vortex footprints at F.S. 142 and F.S. 184 are diminished because the right

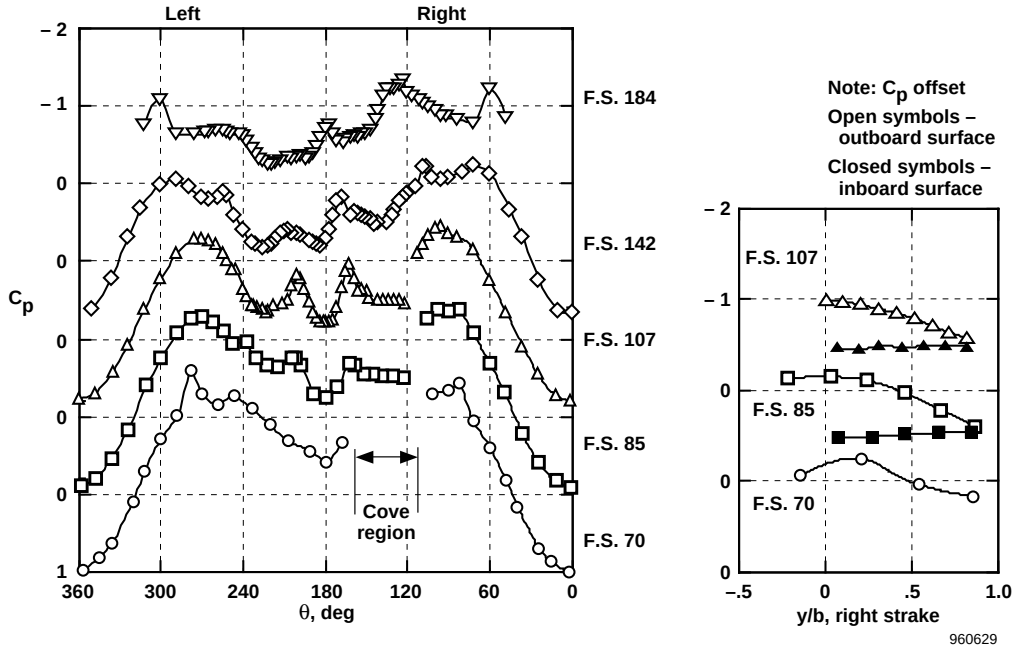

(b) $\delta_{s,\,L/R} = 0°/10°$.

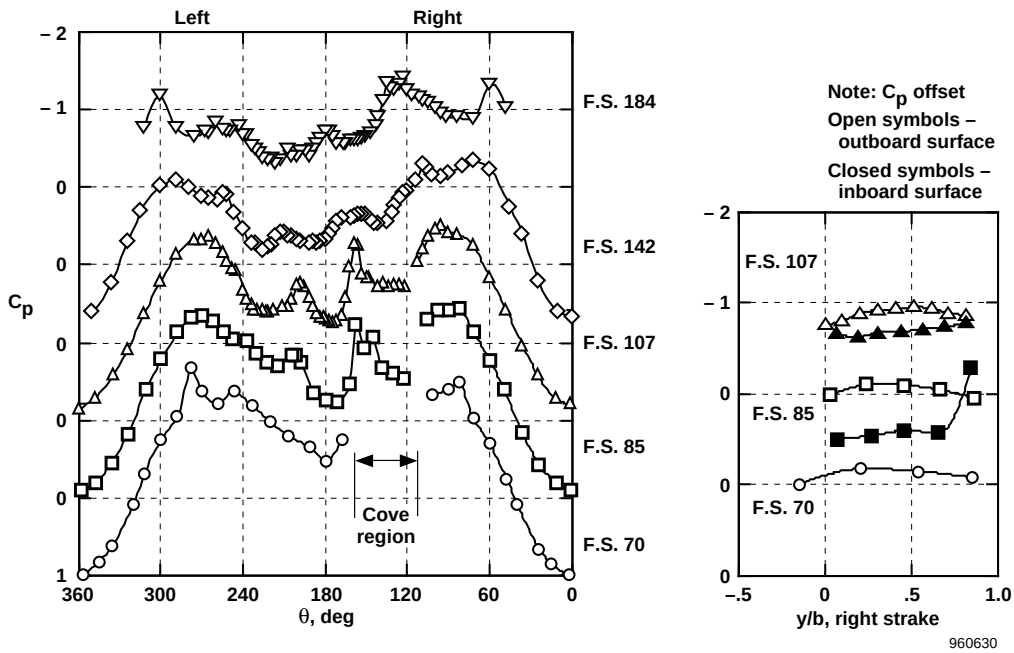

(c) $\delta_{s,\,L/R} = 0°/20°$.

Figure 12. Continued.

vortex is beginning to lift from the forebody surface. Again, the pressures on the right forebody tend to be less than those on the left forebody, particularly at F.S. 142 and F.S. 184. Pressures on the strake are less than ambient, and the outboard surface pressures are generally less than the inboard surface pressures. The suction peak on the inboard surface at $y/b = 0.85$ at F.S. 85 is approximately the same magnitude ($C_p \approx -1.2$) as the one on the right forebody and is caused by the

proximity to the right forebody/strake vortex. Again, the combination of the forebody and strake pressures results in a yawing moment to the right, not the desired direction (figs. 9(c) and 11(a)).

In figure 12(d), the right strake is deflected 30°. This deflection results in a strake that is in a nearly vertical orientation with the fuselage. A large suction peak occurs at $\theta \approx 160°$ at F.S. 85 and is caused by the right forebody/strake vortex. This suction peak diminishes when moving aft on the fuselage and is caused by the vortex lifting from the surface. The forebody vortex on the left, noted by the suction peaks at $\theta \approx 200°$, develops and lifts from the surface later than the right forebody/strake vortex. At F.S. 107, F.S. 142, and F.S. 184, the pressures on the left side at $\theta \approx 240°$ to 300° are generally less than the corresponding pressures on the right side. On the strake, the pressures are all still less than ambient. The suction peak from the strake vortex on the inboard surface at $y/b = 0.85$ has become greater in magnitude ($C_p \approx -1.95$) than the right forebody suction peak ($C_p \approx -1.5$). At F.S. 107, the inboard and outboard strake surface pressures are approximately the same. The net result of the forebody and strake pressure integration is a small yawing moment to the left, the desired direction (figs. 9(c) and 11(a)).

When the right strake extends to 60° (fig. 12(e)), the forebody pressures on the left side at θ = 240° to 300° are noticeably less than the corresponding pressures on the right side for all pressure orifice stations resulting in a yawing moment to the left. At this strake deflection, the strake is approximately 30° out from vertical and retards the flow on the right forebody below the strake. Greater than ambient pressures can be seen on the outboard strake surface at the intersection with the forebody, $y/b \approx 0.2$. The combination of the right and left vortices accelerate the flow around the left forebody as compared to the lower strake deflection angles. The right strake suction peak is a maximum at $\theta \approx 160°$, F.S. 85, and quickly diminishes moving aft as the right forebody/strake

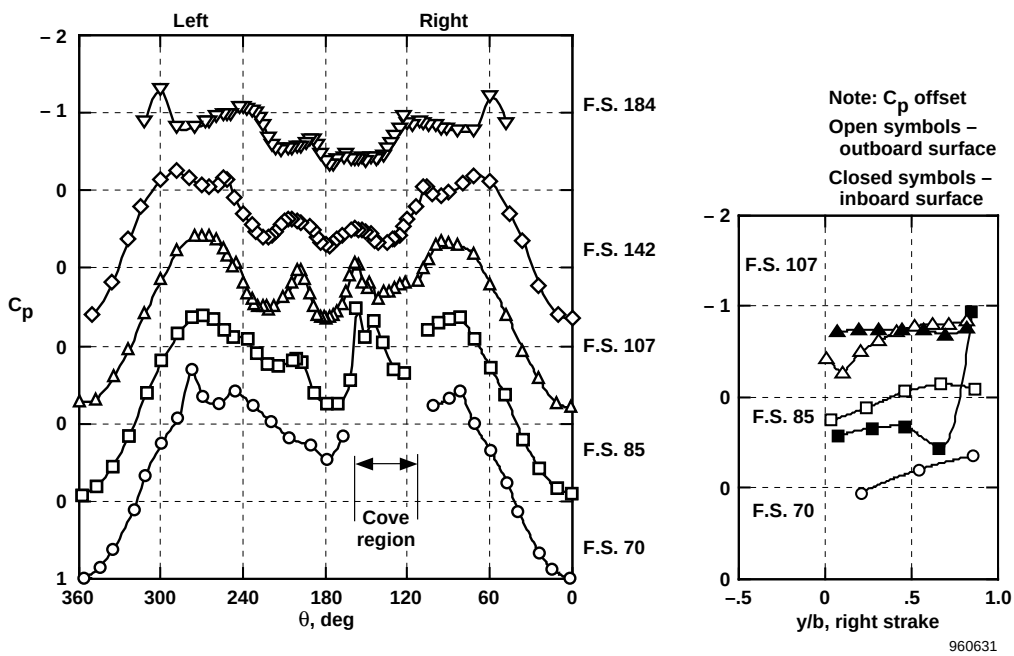

(d) $\delta_{s,\,L/R} = 0°/30°$.

Figure 12. Continued.

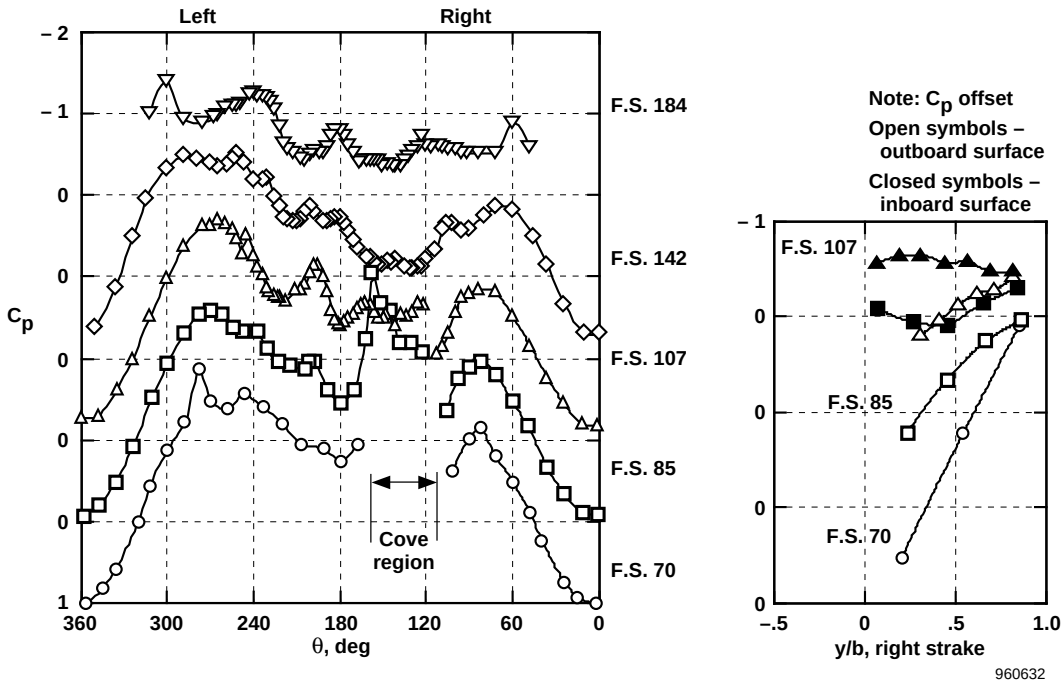

(e) $\delta_{s,\,L/R} = 0°/60°$.

Figure 12. Continued.

vortex lifts from the surface of the radome. The left forebody vortex grows in strength, stays close to the surface, and causes the flow to accelerate around the left side of the forebody. This vortex action results in lower pressures on the left side, hence a yawing moment to the left. The left vortex suction peak is a maximum at $\theta \approx 200°$ at F.S. 107 and moves inboard progressing aft, so this peak is at $\theta \approx 180°$ at F.S. 184. On the strake, pressures on the outboard surface are greater than those on the inboard surface, resulting in a yawing moment to the left. The suction peak ($C_p \approx -2.0$) on the outboard strake surface at F.S. 70, $y/b = 0.85$, is almost the same as for the right vortex suction peak ($C_p \approx -2.1$) at F.S. 85, suggesting that the forebody/strake vortex passes close to that orifice. The sum of large pressure differences on the forebody and strake results in a large yawing moment to the left, (figs. 9(c) and 11(a)).

When the right strake is fully extended to 90° the strake retards the flow below the strake even more than for $\delta_s = 60°$ (fig. 12(f)). The suction peaks at F.S. 70, F.S. 85, and F.S. 107 and $\theta = 60°$ to 120° are significantly lower than for $\delta_s = 60°$ (fig. 12(e)). Pressures on the left side of the fuselage are approximately the same as for $\delta_s = 60°$, (fig. 12(e)). On the strakes at F.S. 85, the difference between the inboard and outboard surface pressures is significantly larger than for $\delta_s = 60°$. Like the $\delta_s = 60°$ case, the pressure distributions indicate that the right vortex lifts from the surface after F.S. 85 while the left vortex stays close to the surface and accelerates the flow around the left side. The suction peak ($C_p = -1.9$) on the inboard strake surface at F.S. 85, $y/b = 0.65$, is almost the same as on the fuselage at the same fuselage station. As a result of the lower suction peaks on the forebody and the outboard and inboard surface pressures on the strake at F.S. 85, the yawing moment to the left was even larger than for $\delta_s = 60°$, (figs. 9(c) and 11(a)).

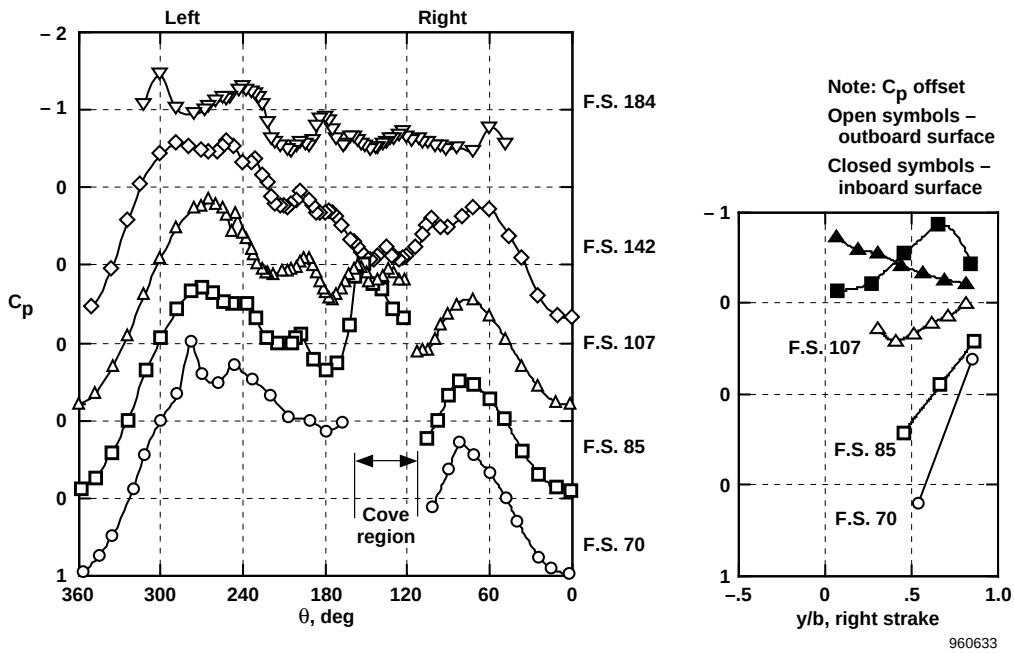

(f) $\delta_{s,\,L/R} = 0°/90°$.

Figure 12. Concluded.

Figure 13 provides supporting evidence of this interpretation, as shown in the wingtip photograph $\alpha = 50°$, $\beta \approx 0°$, and $\delta_{s,\,L/R} = 0°/90°$. The right forebody/strake vortex can be seen very high off the forebody, departing the surface at the strake. A weaker left forebody vortex can be seen lower and near the surface of the forebody.

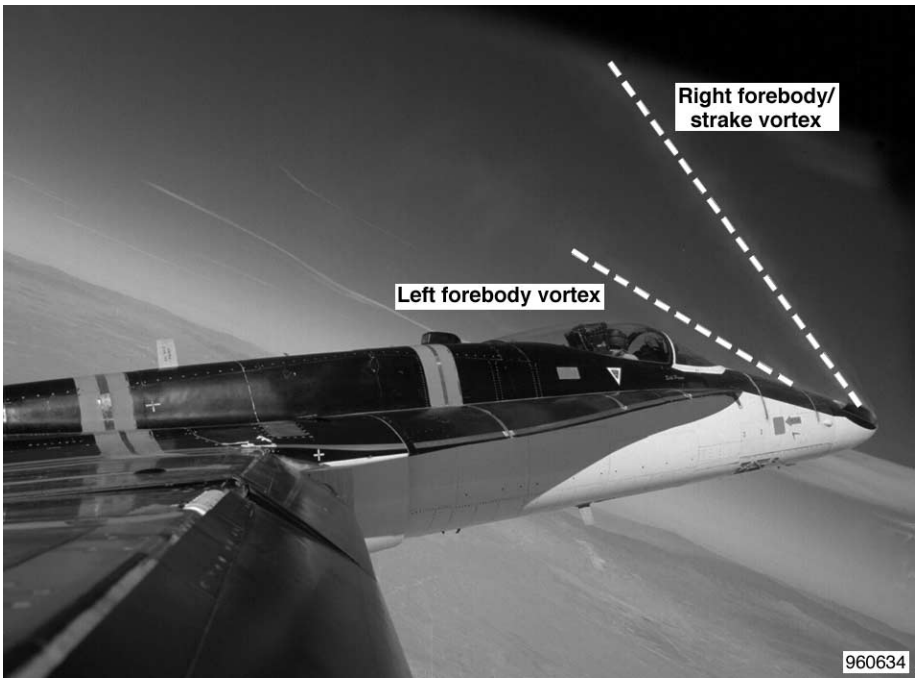

Figure 13. Forebody/strake vortex flow visualization for $\alpha = 50°$ and $\delta_{s,\,L/R} = 0°/90°$.

20° Symmetric Strake Deployment

Symmetric strake deployments were used at high angles of attack to overcome the problem of yaw control reversal at small strake deflections. At $\alpha = 50°$, the 20° symmetric strake deployment yielded the best control linearity characteristics (figs. 9(c) and 11(b)).

Figure 14(a) shows the pressures distributions for $\delta_{s,\,L/R} = 20°/20°$. Compared to the 0° strake deflection case (fig. 12(a)), the suction peaks from the forebody/strakes are slightly more pronounced for F.S. 70, F.S. 85, and F.S. 107. A slight asymmetry exists in the pressure distributions, especially at F.S. 184, with slightly lower pressures on the right side, resulting in a slight yawing moment to the right. No significant differences are seen in the strake pressures from left to right.

For $\delta_{s,\,L/R} = 15°/25°$ (fig. 14(b)), the right forebody/strake vortex suction peak is greater at F.S. 85 than the left but lifts off from the surface sooner, as can be seen by the vortex suction peak pressures at F.S. 142. Except for the suction peaks from the forebody/strake, the forebody pressure distributions from F.S. 70 to F.S. 142 are generally symmetric left to right. At F.S. 184, the pressures on the left side are generally less than those on the right side, resulting in a small yawing moment to the left as desired. The pressures on the outboard side of the strake are generally less than those on the inboard side with the largest difference on the left strake. Again, this difference results in a small net yawing moment to the left.

Figure 14(c) shows a similar trend for $\delta_{s,\,L/R} = 10°/30°$. With the exception of the suction peaks from the forebody/strake vortices, the pressure distributions at F.S. 70 and F.S. 85 are nearly symmetric. As the right forebody/strake vortex suction peak diminishes and the vortex lifts from the surface, the left forebody/strake vortex suction peak increases and the vortex accelerates the flow around the left side of the fuselage resulting in lower pressures on the left side at F.S. 107 to

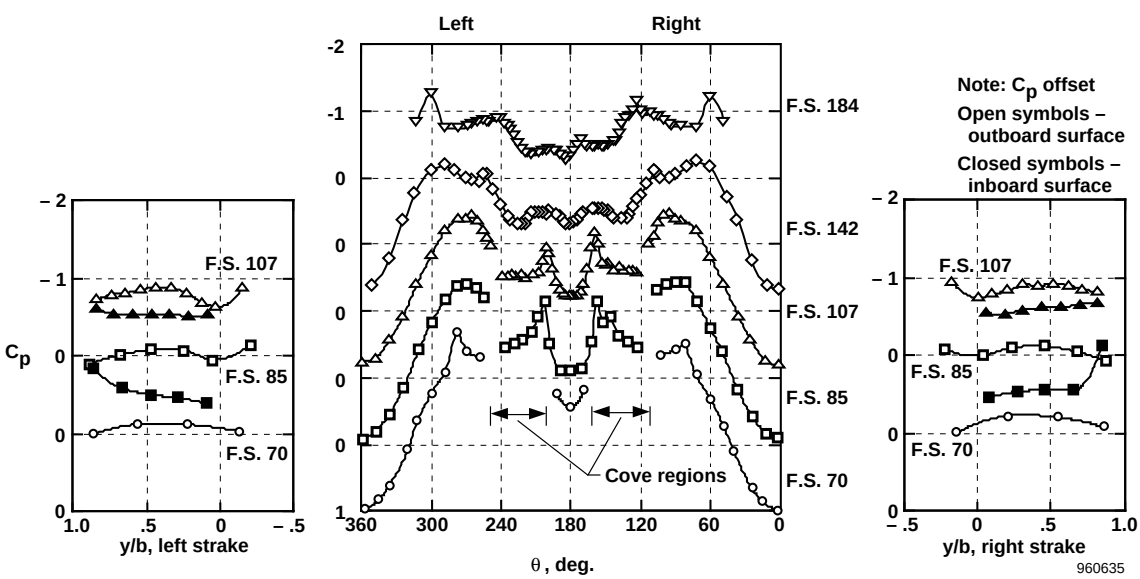

(a) $\delta_{s,\,L/R} = 20°/20°$.

Figure 14. Forebody and strake pressure distributions with the ANSER radome at $\alpha = 50°$ for the 20° symmetric strake deployment, pilots view.

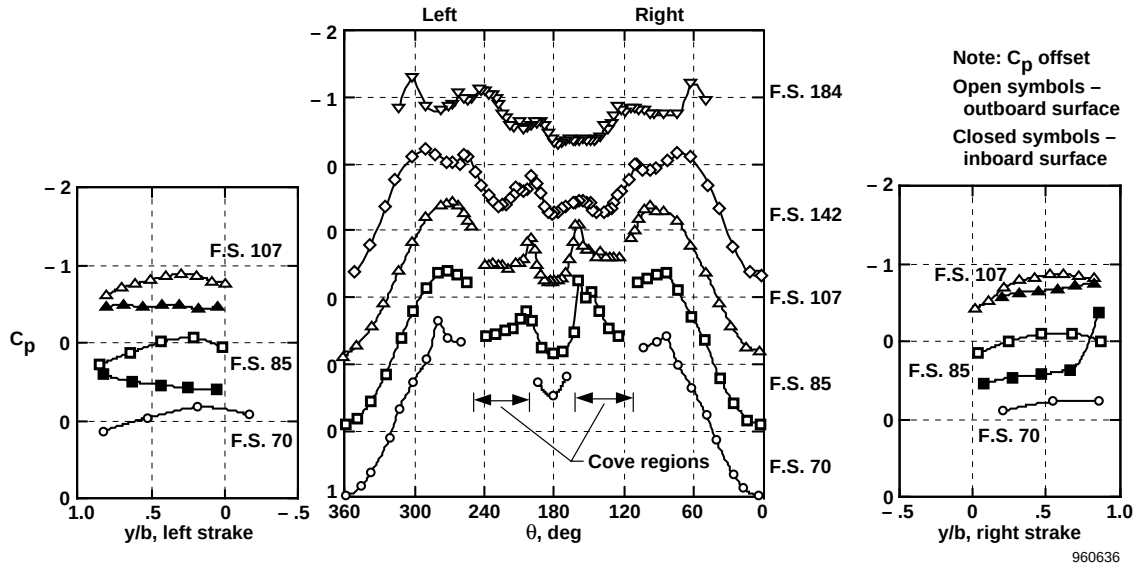

(b) $\delta_{s,\,L/R}$ = 15°/25°.

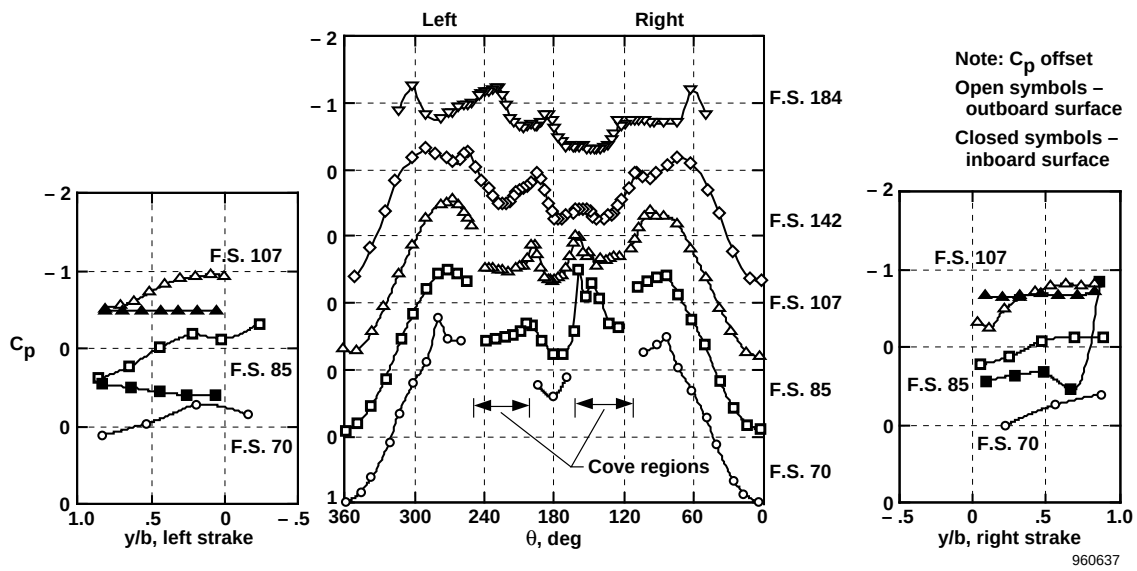

(c) $\delta_{s,\,L/R}$ = 10°/30°.

Figure 14. Continued.

F.S. 184. Note the strength of the left vortex footprint at θ = 200° at F.S. 142 and the left and right side pressures as compared to the same for the 0° symmetric strake deployment, $\delta_{s,\,L/R}$ = 0°/20° case (fig. 12(c)). For the same differential strake deflection of 20°, the left forebody vortex had little beneficial effect. In that case, the dominant right forebody/strake vortex caused the flow to accelerate around the right side of the forebody for all stations aft of F.S. 85, increasing those suction pressures and resulting in a yawing moment to the right. On the strakes for $\delta_{s,\,L/R}$ = 10°/30° the suction peak on the inboard right strake surface at F.S. 85, y/b = 0.85, is caused by the proximity of the forebody/strake vortex as was seen for $\delta_{s,\,L/R}$ = 0°/30° in figure 12(d). Again the outboard strake surface pressures are generally less than the inboard surface pressures with the largest

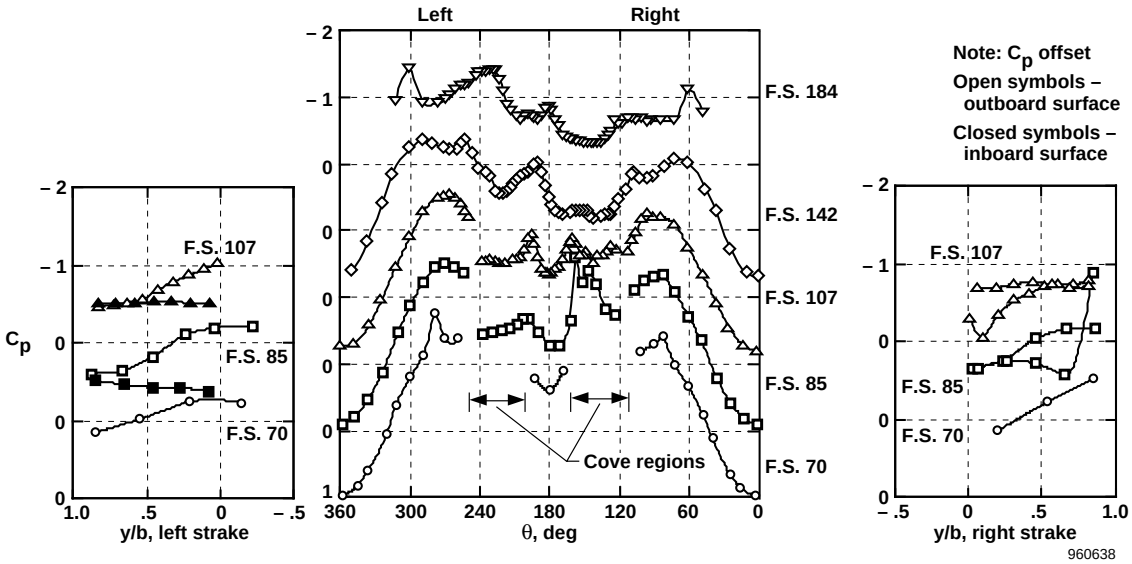

(d) $\delta_{s,\,L/R}$ = 5°/35°.

Figure 14. Concluded.

difference on the left side. Both the forebody and strakes pressure integrations result in yawing moments to the left, (figs. 9(c) and 11(b)).

This same trend continues on for $\delta_{s,\,L/R}$ = 5°/35° (fig. 14(d)). The result of the small left strake deflection is an increase in the strength of the left forebody/strake vortex. For example, the vortex footprint at F.S. 142, θ = 200°, for this strake deflection is much larger than the same differential strake deflection for the 0° symmetric strake deployment, $\delta_{s,\,L/R}$ = 0°/30° (fig. 12(d)). As a result, the stronger left forebody/strake vortex generates lower pressures on the left side and a much larger yawing moment to the left (fig. 9(c)).

As supporting evidence of this analysis, for α = 47°, β = 0.2°, and $\delta_{s,\,L/R}$ = 5°/35°, nearly the same conditions as figure 14(d), figure 15(a) shows the left and right forebody/strake vortices in the wingtip photograph. The right forebody/strake vortex can be seen higher and lifting off the surface sooner. The right vortex stays much closer to the surface and provides the suction needed to accelerate the flow around the left side of the forward fuselage aft of the radome. For comparison, smoke flow visualization is shown in figure 15(b) for the 0° symmetric strake deployment case at $\delta_{s,\,L/R}$ = 0°/27°, α = 50°, and β = –1.4°. For nearly the same differential strake position, only the right forebody/strake vortex close to the surface can be seen. The left vortex does not appear to have a core that can be identified.

Comparison with Wind Tunnel Results

A similar radome with conformal strakes was tested on an F-18 airplane in the NASA Ames Research Center, Moffett Field, California, 80- by 120-Ft Wind Tunnel.[23] This full-scale model had pressure orifices at the same fuselage stations as the HARV. The conformal strakes on this radome, however, did not have the cutouts for the bulkheads that were on the HARV, (fig. 6).

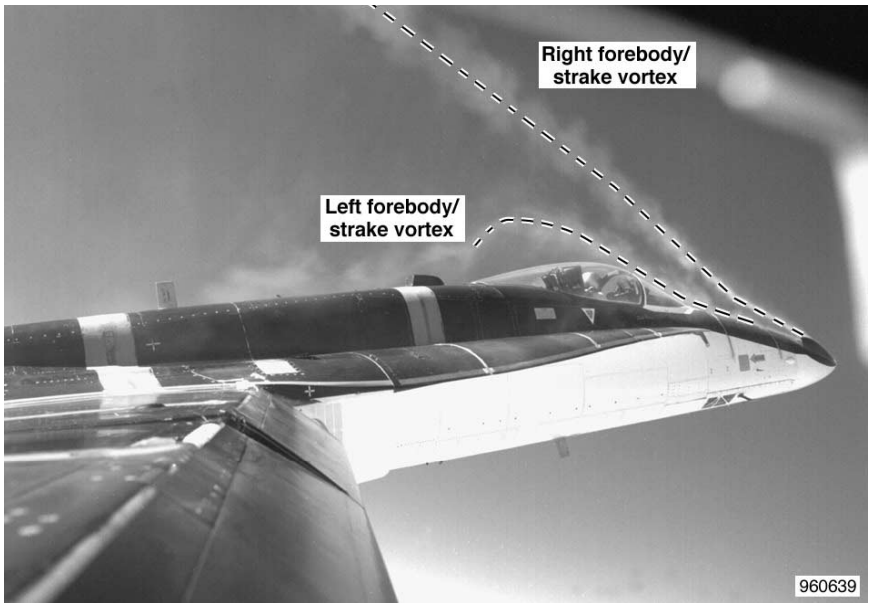

(a) $\delta_{s,\,L/R} = 5°/35°$.

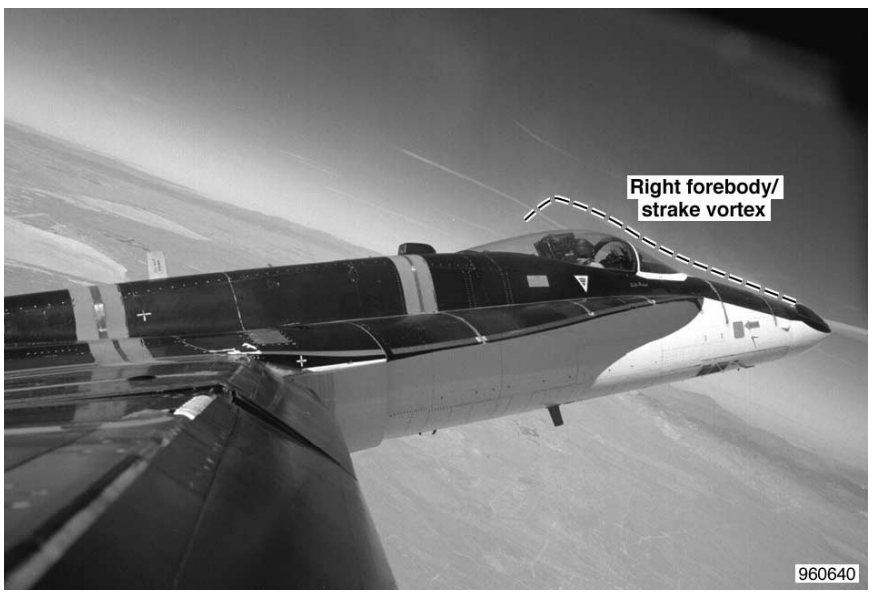

(b) $\delta_{s,\,L/R} = 0°/27°$.

Figure 15. Forebody/strake vortex flow visualization for $\alpha = 50°$ and $\delta_{s,d} \approx 30°$.

Pressure distributions from flight and wind tunnel at $\alpha = 50°$ and $\delta_{s,\,L/R} = 0°/90°$ are compared in figure 16(a). The most obvious difference between flight and the wind-tunnel results is the deficit in the suction peak on the left side ($\theta \approx 240°$ to 280°) starting at F.S. 70 and progressing aft for the flight data. The wind-tunnel data suction peak is much smoother and fuller, similar to previous HARV radome results from flight (fig. 12(a)).[17] The major difference between the wind-tunnel model radome and the ANSER radome was that the large cutouts for the flight ANSER radome were not present on the wind-tunnel model. These cutouts were sealed from the interior of the

radome but not sealed between other cutouts. Axial flow from a region of higher pressure to a region of lower pressure could have existed, thereby affecting the suction peaks at F.S. 70, F.S. 85, and F.S. 107.

On the right side of the fuselage, the pressure distributions from flight and wind tunnel showed good agreement at F.S. 70, F.S. 85, and F.S. 107. At F.S. 142 and F.S. 184, however, the suction pressures on the right side from flight are higher than those from the wind tunnel. The net result is that the wind tunnel has higher forebody yawing moment coefficients for this test condition (fig. 7).

In figure 16(b), flight and wind-tunnel results are compared for $\alpha = 50°$ and $\delta_{s,\,L/R} = 0°/20°$, a condition for which a large yawing moment reversal was noted in flight (fig. 9(c)). Again, at F.S. 70, F.S. 85, and F.S. 107 on the left side, $\theta \approx 240°$ to 280°, the deficit in the flight pressure distributions can be seen compared to the wind-tunnel data. At F.S. 142 and F.S. 184, the wind-tunnel pressures on the left in the region of $\theta = 240°$ to 300° are approximately the same as the corresponding pressures on the right; whereas, those from flight are lower on the right. The net result was a slightly favorable yawing moment to the left for the wind-tunnel data and an unfavorable yawing moment to the right for the flight data, (figs. 9(c) and 10).

Figure 16(c) shows the comparison between flight and wind tunnel data at $\alpha = 50°$ and $\delta_{s,\,L/R} = 10°/30°$, a case where both flight and wind-tunnel data have favorable yawing moments. The flight and wind-tunnel data compare well with the exception of F.S. 142 and F.S. 184 on the right side where the flight pressures are slightly lower. At F.S. 107 on the left strake, the wind-tunnel pressures were slightly lower. No data were obtained at F.S. 85 on the right strake for the wind tunnel.

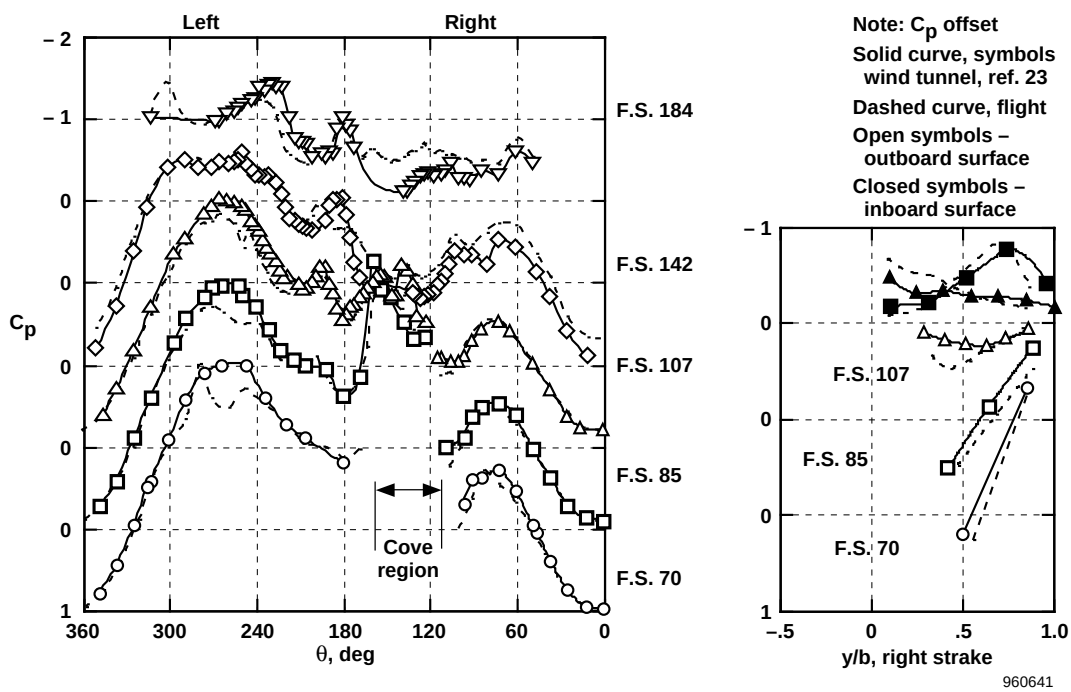

(a) $\delta_{s,\,L/R} = 0°/90°$.

Figure 16. Comparison of flight and wind tunnel pressure distributions, $\alpha = 50°$.

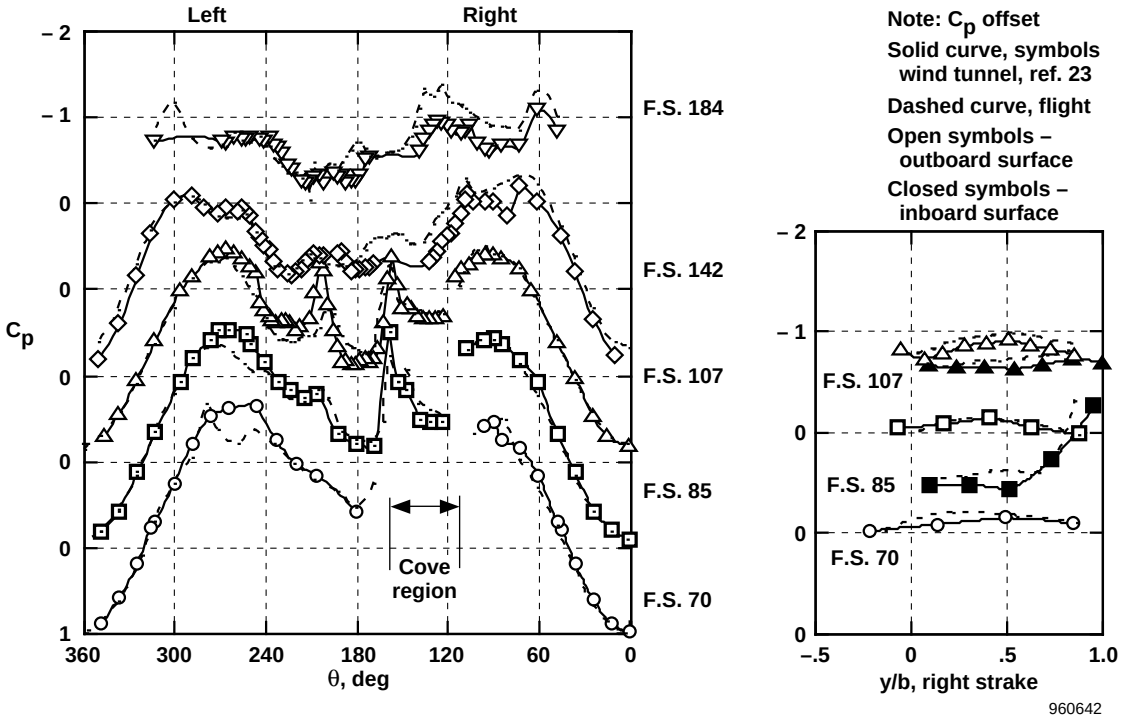

(b) $\delta_{s,\,L/R} = 0°/20°$.

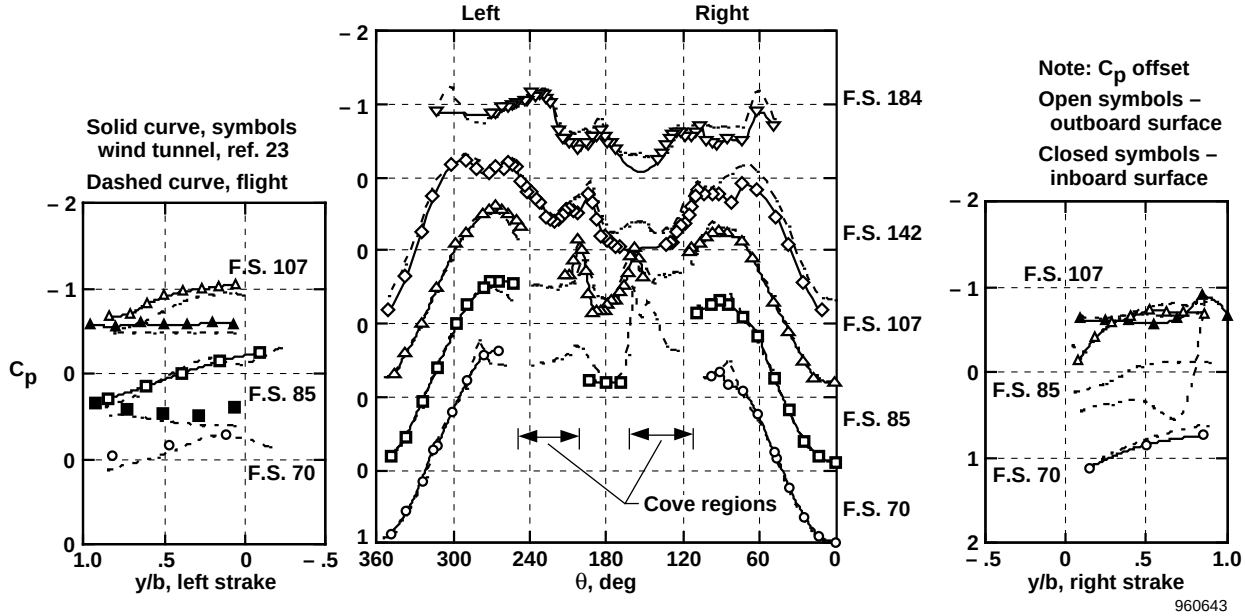

(c) $\delta_{s,\,L/R} = 10°/30°$.

Figure 16. Concluded.

CONCLUDING REMARKS

In-flight pressure distributions have been reported at an angle of attack (α) of 50° at five fuselage stations on the F-18 High-Alpha Research Vehicle (HARV) forebody with actuated forebody strakes. Forebody yawing moments integrated from the forebody pressures were presented at angles of attack of 20°–65°. The results have been correlated with in-flight off-surface flow visualization and wind-tunnel data from the NASA Ames Research Center 80-Ft by 120-Ft Wind Tunnel and the NASA Langley Research Center 30-Ft by 60-Ft Wind Tunnel.

Forebody strakes can generate large yawing moments at high angles of attack. When one strake is deployed fully open, the maximum forebody yawing moment from flight is approximately one-half of the maximum aircraft yawing moment from the wind tunnels. At $\alpha = 50°$, the flight forebody yawing moment is only approximately 80 percent of the wind-tunnel forebody yawing moment. The peak forebody yawing moment from flight was at $\alpha = 55°$ and at $\alpha = 59°$ (maximum test α) for the wind tunnel. Peak forebody yawing moment for the whole airplane from the wind tunnel was at 50°. At $\alpha = 59°$ for the wind tunnel and 65° for flight, the forebody and total aircraft yawing moments from the wind tunnel were approximately equivalent.

At angles of attack of 40° and greater, deflecting one strake at a time resulted in a forebody yawing moment control reversal for small strake deflection angles. At $\alpha = 40°$ and 50°, deflecting the strakes differentially about a 20° symmetric strake deployment eliminated the control reversal and produced a nearly linear variation of forebody yawing moment with differential strake deflection.

When the forebody yawing moments are broken down into radome and forward fuselage yawing moments at $\alpha = 50°$, the major forebody yawing moment is not generated at the region where the strakes are located but rather at the forebody region behind the strakes. At $|\delta_{s,d}| \leq 30°$, the forward fuselage accounts for practically all of the forebody yawing moment.

With the right strake deflections of 10° and 20° and left strake retracted at $\alpha = 50°$, the pressure distributions show that the right forebody/strake vortex was close to the surface. This configuration caused the flow to accelerate around the forward fuselage behind the strake, which resulted in lower pressures on the right side and a forebody yawing moment to the right. For right strake deflections of 60°, the right forebody/strake vortex lifted from the surface of the radome and the left forebody vortex grew in strength and stayed close to the surface. This vortex action caused the flow to accelerate around the left side of the forebody, resulting in lower pressures on the left side and hence a yawing moment to the left.

At $\alpha = 50°$ using the 20° symmetric strake deployment and right strake deflections between 25° and 35°, the deflected left strake increased the strength of the left forebody/strake vortex. This vortex was also closer to the surface than the right forebody/strake vortex and accelerated the flow around the left side, resulting in lower pressures on the left side for all conditions and a forebody yawing moment to the left with no forebody yawing moment control reversal.

A deficit in the suction peaks of the flight pressure distributions was noted just below the undeflected strake as compared to the original HARV radome data and to the wind-tunnel radome data. This deficit was possibly caused by the cutouts in the strakes required for the fuselage bulkheads on the flight hardware.

REFERENCES

[1]Chambers, Joseph R., *High-Angle-of-Attack Technology: Progress and Challenges*, NASA-CP-3149, vol. 1, pt. 2, 1990, pp. 1–22.

[2]Bowers, Albion H. and Pahle, Joseph, "The High Alpha Research Vehicle," High Angle of Attack Conference, NASA Langley Research Center, Sept. 1996.

[3]Chambers, Joseph R., Gilbert, William P., and Nguyen, Luat T., ed, *High-Angle-of-Attack Technology*, vol. 1, pt. 1–3, NASA-CP-3149, vol. 1, 1990.

[4]Matheny, Neil W., comp., *High-Angle-of-Attack Projects and Technology Conference*, NASA-CP-3137, vol. 1, 1992.

[5]*Fourth High Alpha Conference*, NASA-CP-10143, vol. 1, July 1994.

[6]Asbury, Scott C. and Capone, Francis J., *Multiaxis Thrust-Vectoring Characteristics of a Model Representative of the F-18 High Alpha Research Vehicle at Angles of Attack from 0° to 70°*, NASA TP-3531, 1995.

[7]Murri, Daniel G., Biedron, Robert T., Erickson, Gary E., Jordan, Frank L., Jr., and Hoffler, Keith D., *Development of Actuated Forebody Strake Controls for the F-18 High Alpha Research Vehicle*, NASA CP-3149, 1990, pp. 335-380.

[8]Biedron, Robert T. and Thomas, James L., *Navier-Stokes Computations for an F–18 Forebody with Actuated Control Strake*, NASA-CP-3149, vol. 1, pt. 1, 1990, pp. 481–506.

[9]Lanser, Wendy R. and Meyn, Larry A., "Forebody Flow Control on a Full-Scale F/A-18 Aircraft," *J. of Aircraft*, vol. 31, no. 6, 1994, pp. 1365–1371.

[10]Lanser, Wendy R. and Murri. Daniel G., "Wind Tunnel Measurements on a Full-Scale F/A-18 with Forebody Slot Blowing or Forebody Strakes," AIAA 93-1018, 1993.

[11]Pahle, Joseph, Foster, John, Bundick, Tom, and Wichman, Keith, "An Overview of Controls and Flying Qualities Technology on the F/A-18 High Alpha Research Vehicle," High Angle of Attack Conference, Sept. 1996.

[12]Hancock, Regis and Fullerton, Gordon, "X-29 Vortex Flow Control Tests," *Society of Experimental Test Pilots 1992 Report to the Aerospace Profession*, 36th Symposium Proceedings, 1992, pp. 209–219.

[13]Walchli, Lawrence A., "Flight Evaluation of Pneumatic Forebody Vortex Control in Post-Stall Flight, In NASA. Dryden Flight Research Center," Fourth High Alpha Conference, NASA CP-10143, vol. 3, 1994.

[14]Murri, Daniel G, and Rao, Dhanvada M., "Exploratory Studies of Actuated Forebody Strakes for Yaw Control at High Angles of Attack," AIAA 87-2557, 1987.

[15]Murri, Daniel G., Shah, Gautam H., DiCarlo, Daniel J., and Trilling, Todd W., "Actuated Forebody Strake Controls for the F-18 High-Alpha Research Vehicle," *J. of Aircraft*, vol. 32, no. 3, 1995, pp. 555–562.

[16]Moes, Timothy R. and Whitmore, Stephen A., *A Preliminary Look at Techniques Used to Obtain Airdata From Flight at High Angles of Attack*, NASA TM-101729, 1990.

[17]Fisher, David F., Banks, Daniel W., and Richwine, David M., *F-18 High Alpha Research Vehicle Surface Pressures: Initial In-Flight Results and Correlation with Flow Visualization and Wind-Tunnel Data*, NASA TM-101724, 1990.

[18]Curry, Robert E. and Richwine, David M., "An Airborne System for Vortex Flow Visualization on the F-18 High-Alpha Research Vehicle," *AIAA/NASA/AFWAL Sensors and Measurements Technology Conference*, 88-4671-CP, Atlanta, Georgia, Sept. 7–9, 1988.

[19]Fisher, David F., Del Frate, John H., and Richwine, David M., *In-Flight Flow Visualization Characteristics of the NASA F-18 High Alpha Research Vehicle at High Angles of Attack*, NASA TM-4193, 1990.

[20]Fisher, David F. and Lanser, Wendy R., "Flight and Full-Scale Wind-Tunnel Comparison of Pressure Distributions From an F-18 Aircraft at High Angles of Attack," *Fourth High Alpha Conference*, NASA CP-10143, vol. 1, 1994.

[21]Whitmore, Stephen A. and Moes, Timothy R., "The Effects of Pressure Sensor Acoustics on Airdata Derived from a High Angle-of-Attack Flush Airdata Sensing (HI-FADS) System," AIAA 91-0671, Jan. 1991.

[22]Murri, Daniel G., Fisher, David F., and Lanser, Wendy R., "Flight-Test Results of Actuated Forebody Strake Controls on the F-18 High-Alpha Research Vehicle," High Angle of Attack Conference, Sept. 1996.

[23]Lanser, Wendy R., Meyn, Larry A., Botha, Gavin A., James, Kevin D., Hall, Robert M., and Murri, Daniel G., "Overview of Full-Scale F/A-18 Tests in the 80- by 120-ft Wind Tunnel with Small-Scale Comparisons," NASA High Angle of Attack Conference held at Langley Research Center, Sept. 17-19, 1996.

[24]Fisher, David F. and Cobleigh, Brent R., *Controlling Forebody Asymmetries in Flight–Experience with Boundary Layer Transition Strips*, NASA TM-4595, 1994. (see also AIAA-94-1826, July 1994.).

REPORT DOCUMENTATION PAGE

Form Approved
OMB No. 0704-0188

Public reporting burden for this collection of information is estimated to average 1 hour per response, including the time for reviewing instructions, searching existing data sources, gathering and maintaining the data needed, and completing and reviewing the collection of information. Send comments regarding this burden estimate or any other aspect of this collection of information, including suggestions for reducing this burden, to Washington Headquarters Services, Directorate for Information Operations and Reports, 1215 Jefferson Davis Highway, Suite 1204, Arlington, VA 22202-4302, and to the Office of Management and Budget, Paperwork Reduction Project (0704-0188), Washington, DC 20503.

1. AGENCY USE ONLY (Leave blank)

2. REPORT DATE
October 1996

3. REPORT TYPE AND DATES COVERED
Technical Memorandum

4. TITLE AND SUBTITLE
Effect of Actuated Forebody Strakes on the Forebody Aerodynamics of the NASA F-18 HARV

5. FUNDING NUMBERS
WU 505-68-30

6. AUTHOR(S)
David F. Fisher, Daniel G. Murri, Wendy R. Lanser

7. PERFORMING ORGANIZATION NAME(S) AND ADDRESS(ES)
NASA Dryden Flight Research Center
P.O. Box 273
Edwards, California 93523-0273

8. PERFORMING ORGANIZATION REPORT NUMBER
H-2136

9. SPONSORING/MONITORING AGENCY NAME(S) AND ADDRESS(ES)
National Aeronautics and Space Administration
Washington, DC 20546-0001

10. SPONSORING/MONITORING AGENCY REPORT NUMBER
NASA TM-4774

11. SUPPLEMENTARY NOTES
Presented at the NASA Langley High Angle of Attack Technology Conference, Langley Research Center, Sept. 17–19, 1996. David F. Fisher, NASA Dryden Flight Research Center, Edwards, California; Daniel G. Murri, NASA Langley Research Center, Hampton, Virginia; Wendy R. Lanser, Ames Research Center, Moffet Field, California.

12a. DISTRIBUTION/AVAILABILITY STATEMENT
Unclassified—Unlimited
Subject Category 02

12b. DISTRIBUTION CODE

13. ABSTRACT (Maximum 200 words)

Extensive pressure measurements and off-surface flow visualization were obtained on the forebody and strakes of the NASA F-18 High Alpha Research Vehicle (HARV) equipped with actuated forebody strakes. Forebody yawing moments were obtained by integrating the circumferential pressures on the forebody and strakes. Results show that large yawing moments can be generated with forebody strakes. At angles of attack greater than 40°, deflecting one strake at a time resulted in a forebody yawing moment control reversal for small strake deflection angles. At α = 40° and 50°, deflecting the strakes differentially about a 20° symmetric strake deployment eliminated the control reversal and produced a near linear variation of forebody yawing moment with differential strake deflection. At α = 50° and for 0° and 20° symmetric strake deployments, a larger forebody yawing moment was generated by the forward fuselage (between the radome and the apex of the leading-edge extensions), than on the radome where the actuated forebody strakes were located. Cutouts on the flight vehicle strakes that were not on the wind tunnel models are believed to be responsible for deficits in the suction peaks on the flight radome pressure distributions and differences in the forebody yawing moments.

14. SUBJECT TERMS
Angle-of-attack, F-18 aircraft, Flight control, Flight test, Pressure distribution, Vortices, Yawing moments

15. NUMBER OF PAGES
34

16. PRICE CODE
AO3

17. SECURITY CLASSIFICATION OF REPORT
Unclassified

18. SECURITY CLASSIFICATION OF THIS PAGE
Unclassified

19. SECURITY CLASSIFICATION OF ABSTRACT
Unclassified

20. LIMITATION OF ABSTRACT
Unlimited